Contrib Mineral Petrol (2008) 156:133–160
DOI 10.1007/s00410-007-0278-5

ORIGINAL PAPER

Systematics of zircon crystallisation in the Cretaceous Separation Point Suite, New Zealand, using U/Pb isotopes, REE and Ti geothermometry

Robert Bolhar · Steve D. Weaver · J. Michael Palin · Jim W. Cole · Lorraine A. Paterson

Received: 26 April 2007 / Accepted: 21 December 2007 / Published online: 26 January 2008

Abstract Plutonic zircons from the Cretaceous Separation Point Suite (SPS) were analysed by LA-ICPMS for U–Pb isotope ratios and trace element concentrations. Pooled $^{206}Pb/^{238}U$ ages range from 112 to 124 Ma. Cathodoluminescence imaging reveals minor inheritence and textural evidence of repeated dissolution and re-precipitation of zircon. Core and rim spot analyses, however, document zircon growth during extended periods of time (>2 myr). Protracted crystallisation histories for simple plutonic systems are inconsistent with generalised thermal constraints, which predict cooling below the solidus within <1 myr. Consequently, we conclude that the SPS granitoids sampled in this study were not emplaced rapidly but incrementally over extended time periods. Zircon Th/U and Zr/Hf ratios are positively correlated with crystallisation temperatures, consistent with crystallisation from evolving melts. However, highly variable trace element concentrations, along with temperature reversals are indicative of complex crystallisation histories involving continuous fractional crystallisation repeatedly punctuated by hotter, more mafic magma recharge. Normalised abundances of the redox-sensitive elements Eu and Ce in zircon vary systematically with degrees of whole rock differentiation, pointing to evolutionary trends in magmatic oxidation states coupled with feldspar crystallisation.

Keywords ICPMS · Pluton · Separation Point Suite · Ti-in-zircon thermometry · Trace elements · Western Fiordland Orthogneiss · Zircon

Introduction

A large number of geochemical and petrological studies aimed at understanding felsic plutonic and volcanic systems emphasise the fundamental importance of open-system processes for controlling the generation and differentiation of silicic magmas (e.g. Bateman 1995; Robinson and Miller 1999; Wiebe et al. 1997). However, the respective roles of recharge, fractional crystallisation coupled with wallrock assimilation, hybridization and magma source heterogeneity have remained elusive, largely because the compositional make-up of whole rocks can only provide information about the final state of magma prior to eruption or crystallisation deep in the crust. Recent years have seen significant advances in micro-analytical geochemistry directed towards unlocking the isotopic and compositional archives within accessory and major minerals (e.g. Davidson et al. 2001; Francalanci et al. 2005; Gagnevin et al. 2005; Knesel et al. 1999; Ramos and Reid 2005; Tepley et al. 1999). This approach is likely to provide a more detailed record of changing conditions in igneous systems (Davidson et al. 1998), particularly in view of mounting evidence of isotopic, chemical and textural disequilibrium among igneous phases (e.g. Duffield and Ruiz 1992), suggesting their formation at different stages and under changing conditions. Among accessory phases, zircon has proven particularly suitable for tracking

Communicated by T.L. Grove.

R. Bolhar · S. D. Weaver (✉) · J. W. Cole
Department of Geological Sciences, University of Canterbury,
Private Bag 4800, Christchurch 8020, New Zealand
e-mail: steve.weaver@canterbury.ac.nz

R. Bolhar
e-mail: robert.bolhar@canterbury.ac.nz

J. M. Palin · L. A. Paterson
Department of Geology, University of Otago, P.O. Box 56,
Dunedin 9054, New Zealand

magmatic and even metamorphic and hydrothermal processes because internal fine-scaled growth structures are directly correlated with chemical, isotopic and geochronological information encoded within individual grains (e.g. Ballard et al. 2002; Griffin et al. 2002; Hawkesworth and Kemp 2006; Hoskin 2005; Kemp et al. 2005b; Rubatto 2002; Whitehouse and Kamber 2005; Whitehouse and Platt 2003). Recently, Watson et al. (2006) have added to the array of methods a new geothermometer based on the temperature-dependant partitioning of Ti between melt and zircon. This technique allows assessment of the temperatures of magmas from which zircon crystallised (Watson and Harrison 2005).

In the present study LA-ICPMS measurements of U–Th–Pb isotope ratios and trace element abundances, including Ti in zircon, were used to develop new insights into the igneous history of a prominent crustal province in New Zealand, as exemplified by the Separation Point Suite (SPS). Specifically, geochemical and geochronologial information, obtained from the same zircon micro-volume and guided by detailed cathodoluminescence (CL) imaging, is employed to document a complex crystallisation history involving open-system processes and piecemeal construction of plutons. Because the SPS is a major crustal component with a distinct geochemical signature (adakitic or Tonalitic–Trondhjemitic–Granodioritic: TTG), the data presented herein have ramifications for the petrogenesis of plutonic rocks, particularly with reference to suites of adakitic and I-type affinity, and for the generation and differentiation of continental crust in general.

Preliminary results have appeared in abstract form (Bolhar et al. 2006).

Geology

Basement rocks of pre-Mid Cretaceous age constituting the South Island of New Zealand are grouped into three provinces (Bradshaw 1989): the Western Province and the Eastern Province, both separated by the geologically complex Median Tectonic Zone (MTZ) (Fig. 1). The provinces, in turn, consist of a number of fault-bounded terranes, each with its own geologic history (Wandres and Bradshaw 2005). The Western Province is composed predominantly of Palaeozoic metasedimentary rocks, which are intruded by Devonian, Carboniferous and Early Cretaceous granitoids (Muir et al. 1994, 1995, 1998; Waight et al. 1998), and minor volcanic and metamorphic rocks. The Eastern Province comprises arc, forearc and accretionary complex lithologies that were deposited during Permian to Cretaceous place convergence along the eastern Gondwana margin. The MTZ is made up of Carboniferous to Early Cretaceous subduction-related plutonic rocks and lesser quantities of volcanic and sedimentary rocks (Kimbrough et al. 1993, 1994; Mortimer et al. 1999). On the basis of geochronology and geochemistry, granitoids belonging to the MTZ were grouped into the ~170–130 Ma Darran Suite and the ~130–100 Ma SPS (Muir et al. 1994, 1995, 1998), the latter forming the subject of this study. Distinct differences in trace element geochemistry prompted Tulloch and Kimbrough (2003) to classify these suites as LoSY (low Sr/Y ratios) and HiSY (high Sr/Y ratios), respectively. Darran and SPS are generally considered to have formed in a continental arc setting, within and adjacent to the eastern margin of the Western Province (Fig. 1). Proposals have been made to replace the term Median Tectonic Zone with the alternative terms Median Batholith (Mortimer et al. 1999) or Tutoko Complex (Wandres and Bradshaw 2005). However, no consensus has been reached on the use of these terms so here we will continue to use the established term, MTZ.

In Nelson (NW part of the South Island), the Separation Point Batholith comprises three elongate intrusive bodies (northern, central and southern segments) extending in NNE–SSW direction over a length of ~120 km, with an average width of ~10 km. Geobarometry indicates 6–27 km of emplacement depth (Harrison and McDougall 1980; Tulloch and Challis 2000). Field relationships suggest three major (Separation Point Granite, Rocky Granodiorite and Pearse Granodiorite) and one minor phases of emplacement (Fig. 1). Detailed accounts of the petrography and geochemistry of these units were presented by Muir et al. (1995). Lithologically, the Separation Point granites (RNZ20, RNZ49) consist of 15–20% quartz, 30–35% plagioclase, 30–35% orthoclase, 5–10% microcline, 5–10% biotite and 2–3% hornblende. Euhedral titanite, magnetite, zircon, monazite and apatite are accessory phases. In the Rocky Granodiorite and Pearse Granodiorite (biotite–hornblende diorites to granodiorites), plagioclase (An 20–35) forms the dominant felsic mineral, with minor quartz and alkali feldspar present as interstitial phases. Titanite, magnetite, zircon and apatite are accessory phases.

In Fiordland (SW part of the South Island), granitoids, similar in age and composition to the Separation Point Batholith in Nelson, are exposed along the eastern margin of the Western Province within and adjacent to the Darren Suite (Fig. 1). Together, these granitoids comprise the SPS. Three samples (Takahe Granodiorite: SF2a, Titiora Granodiorite: TT6, North Fiord granite: NF3) previously examined by Muir et al. (1998) were chosen in this study to represent the SPS in Fiordland. Early Cretaceous granulite-facies rocks occur in a western belt and are collectively termed the Western Fiordland Orthogneiss (hereafter abbreviated as WFO). Muir et al. (1994) regarded the WFO as the lower crustal equivalents to the SPS. Originally formed 126–114 Ma ago by arc magmatism (Mattinson

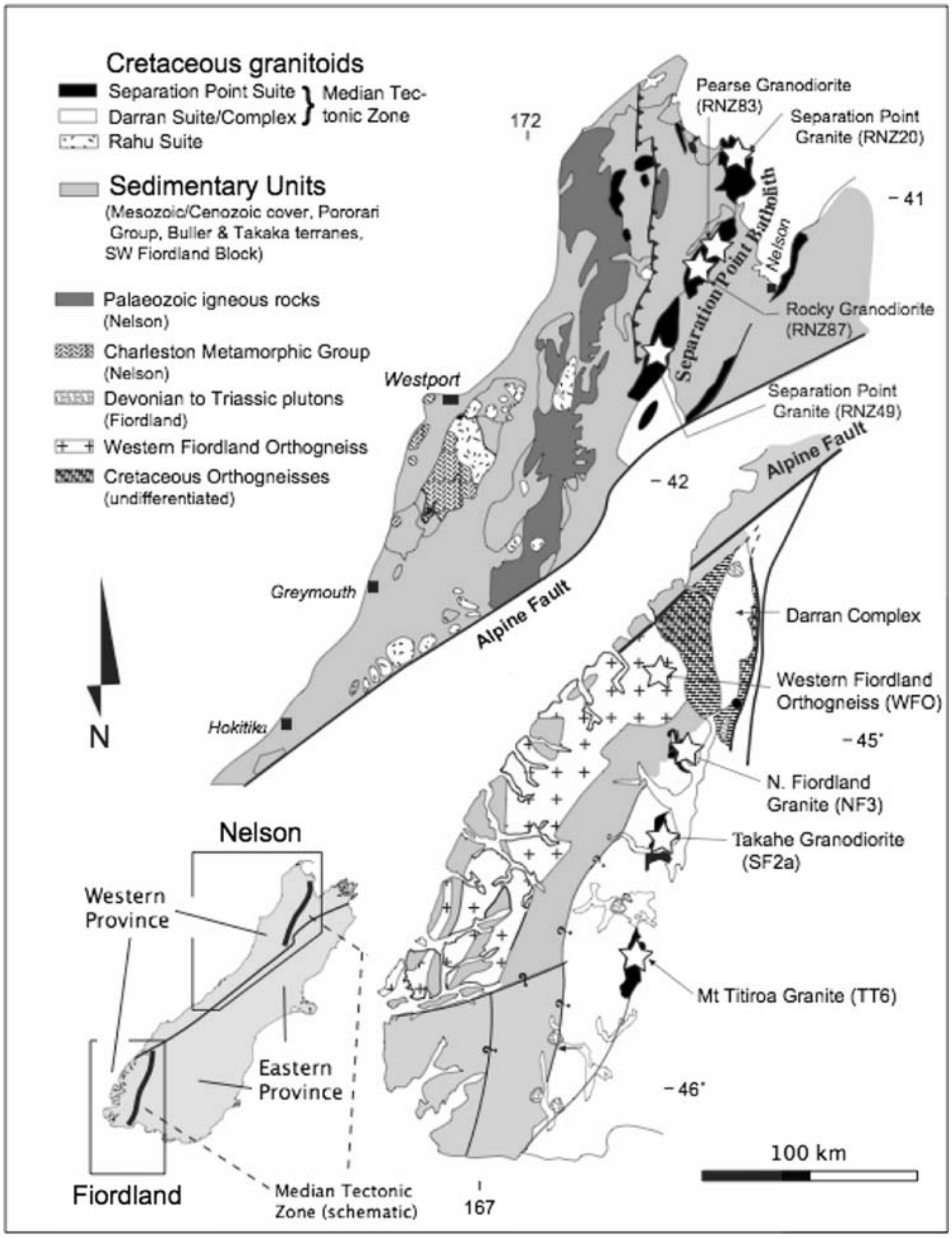

Fig. 1 Geological maps of Nelson and Fiordland showing the distribution of major igneous and sedimentary units; *stars* indicate the location of granitoid samples investigated in this study. The Median Tectonic Zone separating the Western and Eastern Provinces is indicated schematically

et al. 1986; Muir et al. 1998; Hollis et al. 2004), these rocks were subsequently exhumed as deep crustal levels of a metamorphic core complex during continental extension (Gibson and Ireland 1995; Gibson et al. 1988; Scott and Cooper 2006).

Analytical techniques

U–Pb dating

Following routine mineral separation, approximately 100 zircons from each sample were handpicked and mounted in epoxy resin, polished and examined in detail by CL. On the basis of CL images, 20–40 grains were selected for analysis by laser ablation (LA-ICPMS) at the Research School of Earth Sciences, Australian National University, Canberra, following procedures reported by Ballard et al. (2001). Laser ablation utilised a pulsed LambdaPhysik LPX 120I UV ArF excimer laser operated at a constant energy of 70 mJ, at 5 Hz (spot diameter of 24 or 32 µm). Ablated material was transferred by a mixed He–Ar gas from a custom-designed sample cell and flow homogeniser to an Agilent 7500 ICP-MS. Data for 18 mass peaks were collected in time-resolved mode with one point per peak. Due to a relatively high ^{204}Hg blank, ^{204}Pb was excluded. Integration times were: 40 ms for ^{206}Pb, ^{207}Pb, ^{208}Pb, ^{232}Th, ^{235}U, ^{238}U; 10 ms for ^{31}P, ^{89}Y, ^{139}La, ^{140}Ce, ^{147}Sm,

^{153}Eu, ^{163}Dy, ^{175}Lu,^{177} Hf; 5 ms for ^{29}Si, ^{91}Zr and 20 ms for ^{49}Ti. Background data were acquired for 20 s followed by 40 s of laser ablation, yielding about 100 mass scans and a penetration depth of ~20 μm.

Following background substraction and rejection of outliers corrections were applied to each spot analysis for instrumental mass bias and depth-related elemental fractionation. Depth-related inter-element fractionation of Pb, Th, and U were corrected by comparison with standards (TEMORA, NIST610). Measured ^{207}Pb/^{206}Pb, ^{206}Pb/^{238}U, and ^{208}Pb/^{232}Th ratios in the standard zircon and ^{232}Th/^{238}U in the silicate glass standard were averaged over the course of each analytical session and used to calculate correction factors based on accepted values (Black et al. 2003; Pearce et al. 1997).

Internal errors in the isotope ratios for a single spot analysis were calculated from the variation in the corrected isotope ratios for each mass scan across the data interval selected for age calculation. These internal errors were combined with errors estimated from counting statistics for the isotope ratios from each mass scan to calculate within-spot MSWD (mean squared weighted deviates) that were monitored during data interval selection. Spots with resolvable isotopic heterogeneity exhibit internal MSWD values in excess of 5 and were rejected from further consideration in most cases.

Ages were calculated from ^{206}Pb*/^{238}U ratios (where * indicates radiogenic Pb). Common Pb corrections were applied based on the difference between measured and expected ^{208}Pb/^{206}Pb ratios for the measured ^{232}Th/^{238} U value (Compston et al. 1984). Concordance was calculated on the basis of agreement between ^{207} Pb*/^{235}U and ^{206}Pb*/^{238}U ages.

Uncertainties in the ^{206}Pb*/^{238}U ages of individual spot analyses take into account errors for each of the isotope ratios used for geochronology based on the SD in the same isotope ratios measured in the TEMORA zircon standard over the course of each analytical session (typically 1–2%). Compared with these errors, the reported error in the age of the TEMORA zircon standard is negligible (Black et al. 2003). Uncertainties in pooled ^{206}Pb*/^{238}U ages are reported at the 2 standard error (SE) level.

During three analytical sessions, 45 spot analyses of the reference zircon 91500 were made as unknowns. All analyses were concordant to near-concordant (97–103% concordance), and yielded an error weighted mean ^{206}Pb/^{238}U age of 1,056.4 ± 6.2 (2σ) (Fig. 2a), identical within errors to the ^{206}Pb/^{238}U age of 1,062.4 ± 0.4 Ma obtained by TIMS (Wiedenbeck et al. 1995). Calculated ages from each session lie within uncertainty of each other: 1,055 ± 14 Ma ($N = 15$), 1,052 ± 16 Ma (12) and 1,059 ± 8 ($N = 18$) Ma. Thus, in this study, the ^{206}Pb/^{238}U age of the reference zircon 91500 was determined at levels of accuracy and precision of <1%. Scatter in ages for 91500 (Fig. 2a) may be attributed to inhomogeneity of the standards used for depth-related fractionation correction and instrumental drift.

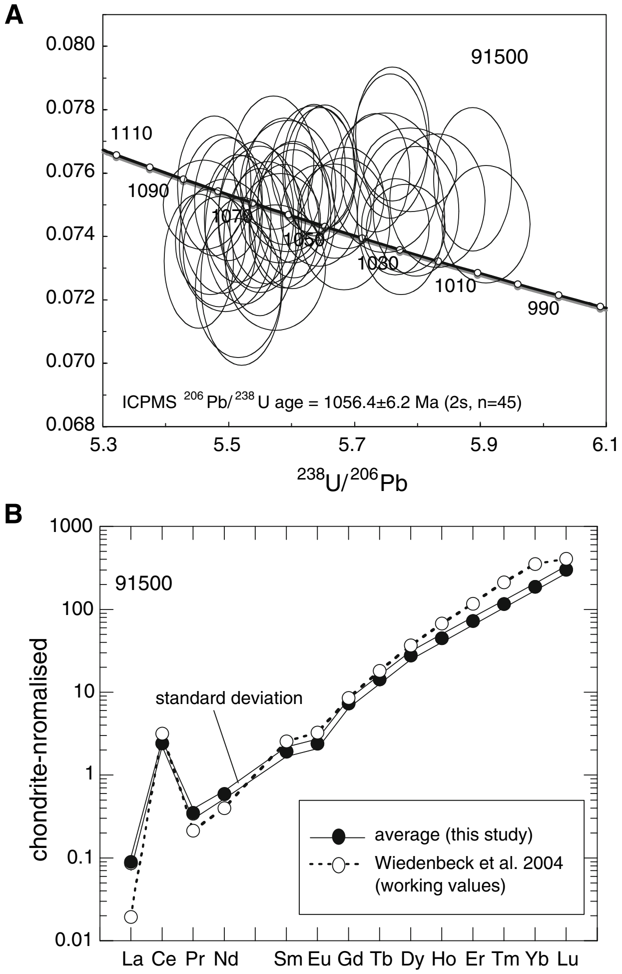

Fig. 2 **a** Tera-Wasserburg concordia diagram showing uncorrected (common Pb) U–Pb isotope data for zircon standard 91500. Data error point ellipses are 2σ. **b** Rare earth element (*REE*) analytical data (chondrite-normalised using the values from Boynton 1984) for zircon standard 91500 from this study (average of 45 analyses). Note the good agreement with working values of Wiedenbeck et al. (2004) for Ce, Sm, Eu and Lu. ICMPS values for La are considerably lower than the published working value, probably reflecting insufficiently low detection levels for the La concentration levels encountered in zircon

Trace elements

Data for P, Ti, Y, Zr, La, Ce, Sm, Eu, Dy, Lu, and Hf were acquired simultaneously with the U–Pb isotope measurements. Raw data were converted to concentrations (in parts per million) by normalising count rates for each element to those for Si, assuming SiO_2 to be stoichiometric in zircon with a concentration of ca. 32.8 wt%, and multiplying by a correction factor based on concurrent measurement of standard glass NIST 610 with concentration values recommended by Pearce et al. (1997).

The laser ablation spots in zircon are carefully selected to avoid mineral and glass inclusions, inherited cores, and cracks, and most grains displayed smooth elemental patterns. However, it is difficult to avoid all sub-surface heterogeneities. Apatite is a common inclusion that can strongly perturb LREE concentrations in zircon. To monitor for apatite inclusions, phosphorus was included in the list of elements measured. Zircons with high P count rates almost always displayed correspondingly high levels of LREE, usually within discrete depth intervals, consistent with the apatite inclusion hypothesis. These data intervals were excluded from age and concentration calculations.

Spot analyses of 91500 by LA-ICPMS also included the above set of trace elements. Analytical errors (expressed as relative SDs calculated from the 45 analyses) are ±6% (HfO_2), ±11% (P, Y), ±8% (Ti), ±17% (La), ±9% (Ce), ±13% (Sm, Eu), ±12% (Dy) and ±10% (Lu). Chondrite-normalised rare earth element (REE) patterns of 91500 measured in this study (average of 45 analyses) are compared with working values recommended by Wiedenbeck et al. (2004) in Fig. 2b. Values for Pr, Nd, Gd, Tb, Dy, Ho, Er, Tm were calculated through interpolation using the following equations: $\mathrm{Pr} = 10^{(3/5\log\mathrm{La} + 2/5\log\mathrm{Sm})}$, $\mathrm{Nd} = 10^{(2/3\log\mathrm{Pr} + 1/3\log\mathrm{Sm})}$, $\mathrm{Gd} = 10^{(1/2\log\mathrm{Sm} + 1/2\log\mathrm{Dy})}$, $\mathrm{Tb} = 10^{(1/2\log\mathrm{Gd} + 1/2\log\mathrm{Dy})}$, $\mathrm{Ho} = 10^{(0.8\log\mathrm{Dy} + 0.2\log\mathrm{Lu})}$, $\mathrm{Er} = 10^{(0.6\log\mathrm{Dy} + 0.4\log\mathrm{Lu})}$, $\mathrm{Tm} = 10^{(0.4\log\mathrm{Dy} + 0.6\log\mathrm{Lu})}$, $\mathrm{Yb} = 10^{(0.2\log\mathrm{Dy} + 0.8\log\mathrm{Lu})}$.

$\mathrm{Ti}_{\mathrm{zircon}}$ thermometry

Watson et al. (2006) have recently devised a thermometer, based on the temperature dependant incorporation of Ti^{4+} into crystallising zircon under TiO_2-saturated conditions (i.e. rutile is present). Assuming a TiO_2 activity of 1 and using Ti concentrations obtained by LA-ICPMS, $T_{\mathrm{crystalliation}}$ were calculated according to: $T\,(°\mathrm{C}) = [(5{,}080 \pm 30)/(6.01 \pm 0.03) - (\log\,(\mathrm{Ti})] - 273$ (Eq. 7 of Watson et al. 2006). Crystallisation temperatures are reported in Tables 1 and 2. Uncertainty pertinent to calculating $T_{\mathrm{crystalliation}}$ with the Ti-in-zircon thermometer ("calibration uncertainty") has been estimated by Watson et al. (2006) at $<10°\mathrm{C}$ (2σ) for the temperature range observed in this study. Uncertainty in the order of 10% (relative SD calculated from 45 analyses of standard 91500, see above) arising from LA-ICMPS analysis of Ti concentrations translates into uncertainties of ca. 10°C. As noted by Ferry and Watson (2007), uncertainties due to activities of TiO_2 and SiO_2 less than 1 during zircon crystallisation tend to offset one another.

Results

Cathodoluminescence imaging and U/Pb geochronology

In the following discussion, the innermost identifiable zones within zircons are referred to as cores, irrespective of whether they are inherited based on dates that are significantly older than the supposed crystallisation age of the host rock. Rims are defined as representing material enclosing the inner portions. During analysis, emphasis was placed on selecting a wide variety of zircons with differing sizes, morphologies and internal make-up in order to minimise sampling bias. U–Th–Pb isotope and U, Th, Pb elemental data are reported in Tables 1 (Nelson) and 2 (Fiordland). Catholuminescence images are given in Fig. 3; Tera-Wasserburg diagrams showing U–Pb isotope data for individual zircon spot analyses are presented in Fig. 4.

Northwest Nelson

Separation point granite/N-segment (RNZ20)

Zircons are typically 200–300 µm in length, euhedral, short to long prismatic, with aspect ratios of 1:2 to 1:4. The majority of grains lack discernible, inherited cores, but, where preserved, cores are rounded, zoned and distinct from enclosing rims by virtue of luminescence and truncated zoning. Oscillatory zoning is the prominent textural feature, with growth bands varying between fine and broad within individual grains. Luminescence of growth zoning is variable and mostly moderate. Grains often have irregular margins and embayments indicative of corrosion. Minor quantities of mineral inclusions are apparent.

Thirteen spot analyses (all >90% concordant) yield $^{206}\mathrm{Pb}^*/^{238}\mathrm{U}$ dates of 108–124 Ma, with three inherited cores having significantly older dates of 133 ± 2, 288 ± 24 and 463 ± 10 Ma. Interior and exterior domains give weighted mean ages of 114.4 ± 4.8 Ma ($\mathrm{MSWD} = 3.3$, $N = 3$) and 112.1 ± 2.0 Ma ($\mathrm{MSWD} = 1.6$, $N = 8$), respectively. Two dates (122, 124 Ma) are considered to represent subtle inheritance (see discussion below) and are excluded from age calculation. The pooled age of 112.7 ± 1.9 Ma ($\mathrm{MSWD} = 1.9$, $N = 11$) is slightly younger than the SHRIMP age of 116.6 ± 1.9 Ma published by Muir et al. (1994).

Separation point granite/S-segment (RNZ49)

Zircons (~100–200 µm, aspect ratios 1:2 to 1:3) are subhedral to euhedral and long to short-prismatic. Most grains

Table 1 U-Th-Pb isotope and Ti concentration data for zircons from Separation Point granitoids (Nelson)

Analysis	Domain	Pb* (ppm)	U (ppm)	Atomic Th/U	Measured isotope ratios and 1 s (%) internal errors								Corrected ages (Ma) and absolute internal errors (1 s)							Selected age (Ma)	±	Ti (ppm)	*T* (°C)
					206Pb/ 238U	±	207Pb/ 235U	±	207Pb/ 206Pb	±	208Pb/ 232Th	±	206Pb*/ 238U	±	207Pb*/ 235U	±	Concord-ance (%)	Common 206Pb (%)	Spot MSWD				
Separation Point Granite N-segment																							
RNZ20-03	c	1.74	79	0.64	0.01977	1.2	0.2282	5.8	0.0837	5.7	0.00879	4.6	121.8	1.6	124.7	17.1	98	4.14	2.1			3.91	665
RNZ20-04	r	2.87	154	0.50	0.01770	0.7	0.1208	2.7	0.0495	2.5	0.00601	1.5	112.9	0.8	104.4	4.4	108	0.59	2.0	112.9	2.2	2.24	624
RNZ20-05	r	4.16	212	0.70	0.01777	0.6	0.1207	2.5	0.0492	2.5	0.00558	1.2	114.3	0.7	116.9	4.0	98	−0.07	2.1	114.3	2.2	bdl	
RNZ20-06	c	7.21	291	0.92	0.02127	0.9	0.2293	6.1	0.0782	6.0	0.00760	2.7	133.0	1.8	146.7	25.1	91	2.91	9.6			14.48	775
RNZ20-07	c	3.11	126	1.16	0.01968	1.0	0.1570	3.6	0.0578	3.4	0.00699	1.7	123.9	1.5	93.1	14.9	133	2.60	2.8			4.76	680
RNZ20-08	r	4.79	233	1.00	0.01729	0.6	0.1243	2.7	0.0521	2.6	0.00543	1.1	111.6	0.7	121.9	5.5	92	−0.16	2.2	111.6	2.1	bdl	
RNZ20-09	c	3.35	165	1.04	0.01698	0.7	0.1145	2.8	0.0489	2.7	0.00521	1.1	110.1	0.9	121.6	5.9	90	−0.63	2.5	110.1	2.2	3.55	657
RNZ20-10	r	3.08	154	0.72	0.01806	0.8	0.1246	2.7	0.0500	2.6	0.00568	1.4	115.9	1.3	122.9	15.9	94	−0.19	2.4	115.9	2.5	bdl	
RNZ20-11	c	8.34	160	0.83	0.04532	8.3	0.3733	8.6	0.0597	2.4	0.01466	9.1	288.1	23.4	329.1	34.2	88	−0.17	194			3.09	647
RNZ20-12	r	4.62	233	0.51	0.01837	1.3	0.1768	2.9	0.0698	2.6	0.00802	3.6	115.0	1.5	115.1	8.0	100	2.59	6.6	115.0	2.6	28.57	842
RNZ20-13	c	2.20	99	0.98	0.01854	0.9	0.1223	3.6	0.0478	3.4	0.00638	1.6	117.5	1.3	82.4	13.8	143	1.71	2.3	117.5	2.5	5.09	685
RNZ20-14	r	1.47	78	0.58	0.01760	0.8	0.1101	4.1	0.0454	4.0	0.00555	2.1	112.9	0.9	106.0	5.8	107	0.00	5.0	112.9	2.3	3.70	661
RNZ20-17	c	7.53	318	1.33	0.01836	0.9	0.1542	3.2	0.0609	3.1	0.00619	1.3	117.0	1.3	116.2	13.3	101	1.51	3.8	117.0	2.5	4.19	670
RNZ20-18	r	3.86	204	0.70	0.01707	0.6	0.1232	2.4	0.0523	2.3	0.00555	1.4	109.5	0.7	112.5	4.2	97	0.29	1.9	109.5	2.1	3.52	657
RNZ20-19	c	44.93	546	0.72	0.07397	1.1	0.5859	1.4	0.0574	0.8	0.02273	1.6	463.2	5.1	478.0	8.8	97	−0.17	41			6.49	704
RNZ20-20	r	6.69	326	1.12	0.01671	0.6	0.1170	1.8	0.0508	1.7	0.00536	0.9	107.6	0.7	107.7	4.7	100	0.26	3.2	107.6	2.1	3.08	647
Separation Point Granite S-segment																							
RNZ49-01	c	57.39	322	0.43	0.17039	0.4	1.7210	0.7	0.0733	0.5	0.05182	0.6	1016.5	4.0	1011.7	5.9	100	0.06	9.7			5.38	689
RNZ49-02	r	4.59	288	0.20	0.01635	0.8	0.1287	2.7	0.0571	2.6	0.00720	4.3	103.7	0.8	105.0	3.8	99	1.01	2.4			2.72	638
RNZ49-03	r	14.77	839	0.37	0.01735	0.4	0.1133	1.3	0.0474	1.2	0.00552	0.9	111.2	0.5	108.5	1.7	102	0.02	3.2	111.2	2.1	2.97	644
RNZ49-04	c	22.47	1097	0.73	0.01813	1.1	0.1217	1.5	0.0487	1.1	0.00657	2.1	114.1	1.6	76.2	17.9	150	2.03	16	114.1	2.6	bdl	
RNZ49-05	c	20.64	215	0.42	0.09313	0.9	0.7423	1.2	0.0578	0.8	0.02860	1.4	573.4	5.2	549.2	18.6	104	0.22	14			3.72	661
RNZ49-06	r	10.46	551	0.40	0.01839	0.6	0.1301	1.5	0.0513	1.4	0.00690	1.2	116.5	0.7	99.8	4.0	117	1.22	4.2	116.5	2.2	bdl	
RNZ49-07	c	14.45	784	0.69	0.01669	0.6	0.1106	1.5	0.0481	1.4	0.00527	0.9	107.4	0.8	108.2	7.2	99	−0.09	6.3	107.4	2.1	5.11	685
RNZ49-08	r	34.50	2082	0.66	0.01512	0.4	0.1015	0.9	0.0487	0.8	0.00486	0.7	97.1	0.4	96.0	2.2	101	0.13	8.3			5.77	695
RNZ49-09	r	7.15	352	0.68	0.01843	1.2	0.1252	2.3	0.0493	2.0	0.00574	1.4	118.6	1.5	125.1	8.5	95	−0.27	7.9	118.6	2.6	bdl	
RNZ49-10	c	5.76	288	0.73	0.01775	0.7	0.1390	2.7	0.0568	2.6	0.00624	1.6	112.8	0.8	109.6	7.4	103	1.18	2.7	112.8	2.2	bdl	
RNZ49-11	c	105.45	768	0.45	0.12985	5.6	1.7082	5.7	0.0954	1.1	0.05189	5.2	774.8	40.8	878.4	37.7	88	2.05	4154			7.73	719
RNZ49-12	r	14.86	845	0.38	0.01731	0.7	0.1146	1.3	0.0480	1.1	0.00561	1.3	110.8	0.8	107.4	2.7	103	0.14	8.4	110.8	2.2	3.46	656
RNZ49-13	r	3.30	189	0.36	0.01712	0.8	0.1137	2.6	0.0482	2.5	0.00643	2.7	108.6	1.1	90.2	11.9	120	1.02	2.1	108.6	2.2	bdl	
RNZ49-14	c	2.36	131	0.48	0.01732	0.8	0.1117	3.1	0.0468	3.0	0.00534	2.2	111.3	0.9	111.6	4.6	100	−0.21	1.8	111.3	2.2	2.36	628
RNZ49-15	c	3.28	163	0.79	0.01776	0.7	0.1287	2.3	0.0525	2.2	0.00580	1.6	113.6	0.9	112.9	6.5	101	0.52	2.1	113.6	2.2	bdl	
RNZ49-16	r	9.33	532	0.32	0.01750	0.7	0.1284	1.7	0.0532	1.5	0.00611	1.3	111.6	0.7	113.0	2.3	99	0.51	4.7	111.6	2.1	bdl	
RNZ49-17	c	9.23	467	0.35	0.01957	3.8	0.1382	4.2	0.0512	1.6	0.00653	4.2	125.0	4.8	126.2	5.8	99	0.25	45			5.09	685
RNZ49-18	r	17.98	1064	0.47	0.01622	0.7	0.1168	1.6	0.0522	1.5	0.00522	1.6	104.0	0.7	109.8	3.5	95	0.14	6.7			3.87	664
Separation Point: Pearce Granodiorite																							
RNZ83-01	c	2.20	105	0.85	0.01826	0.8	0.1170	3.3	0.0464	3.2	0.00578	1.7	118.1	1.2	113.5	12.5	104	−0.06	1.5	118.1	2.4	10.20	743
RNZ83-03	c	4.07	180	1.09	0.01865	0.8	0.1232	2.8	0.0479	2.7	0.00575	1.3	120.6	1.1	125.0	6.8	97	−0.35	3.3	120.6	2.4	9.32	735

Table 1 continued

Analysis	Domain	Pb* (ppm)	U (ppm)	Atomic Th/U	Measured isotope ratios and 1 s (%) internal errors								Corrected ages (Ma) and absolute internal errors (1 s)							Selected age (Ma)	±	Ti (ppm)	*T* (°C)
					206Pb/ 238U	±	207Pb/ 235U	±	207Pb/ 206Pb	±	208Pb/ 232Th	±	206Pb*/ 238U	±	207Pb*/ 235U	±	Concord-ance (%)	Common 206Pb (%)	Spot MSWD				
RNZ83-04	r	11.27	549	0.71	0.01855	0.7	0.1210	2.5	0.0473	2.4	0.00567	1.1	119.6	1.4	123.5	18.1	97	−0.38	4.7	119.6	2.6	5.80	695
RNZ83-05	r	3.91	206	0.70	0.01713	0.7	0.1198	3.3	0.0507	3.3	0.00546	1.8	110.1	0.8	113.4	6.2	97	0.08	1.1			9.41	736
RNZ83-06	c	7.50	444	0.22	0.01730	0.6	0.1301	1.9	0.0546	1.8	0.00676	1.7	109.9	0.7	109.5	2.7	100	0.79	3.2			4.79	680
RNZ83-07	c	4.74	251	0.38	0.01861	0.6	0.1186	2.0	0.0462	1.9	0.00574	1.5	119.4	0.7	117.1	2.9	102	−0.16	2.0	119.4	2.3	4.07	668
RNZ83-08	r	2.43	110	0.93	0.01892	0.9	0.1222	4.1	0.0468	4.0	0.00577	1.7	122.1	1.2	125.4	10.2	97	−0.41	1.9	122.1	2.5	10.94	749
RNZ83-09	r	2.89	151	0.79	0.01682	1.1	0.1569	3.5	0.0676	3.3	0.00607	2.1	106.3	1.2	113.5	7.7	94	1.93	2.3			6.40	703
RNZ83-10	c	6.44	279	1.33	0.01797	0.5	0.1157	2.2	0.0467	2.1	0.00567	0.7	116.2	0.7	112.0	6.9	104	−0.04	2.7	116.2	2.2	15.63	782
RNZ83-11	c	3.45	155	1.18	0.01803	0.8	0.1230	2.9	0.0495	2.8	0.00553	1.0	117.0	1.0	128.5	6.3	91	−0.55	2.5	117.0	2.3	12.94	764
RNZ83-12	r	3.62	172	0.90	0.01812	0.8	0.1258	2.8	0.0503	2.7	0.00579	1.3	116.4	1.0	117.9	7.0	99	0.12	2.4	116.4	2.3	11.65	755
Separation Point: Rocky Granodiorite																							
RNZ87-01	r	1.94	100	0.64	0.01785	0.9	0.1160	3.7	0.0472	3.5	0.00566	1.5	114.5	1.1	109.6	5.5	104	0.09	2.2	114.5	2.3	5.68	694
RNZ87-02	c	1.27	61	0.78	0.01852	1.0	0.1287	4.5	0.0504	4.4	0.00578	2.0	119.1	1.2	124.5	8.1	96	−0.08	1.5	119.1	2.5	10.15	742
RNZ87-03	c	6.20	287	0.55	0.02038	1.1	0.1346	2.2	0.0479	1.9	0.00622	1.5	130.9	1.4	133.1	3.6	98	−0.23	5.0			3.97	666
RNZ87-04	r	3.13	174	0.26	0.01821	1.0	0.1392	3.7	0.0554	3.5	0.00696	2.6	115.6	1.2	115.5	6.6	100	0.87	2.4	115.6	2.4	3.61	659
RNZ87-05	r	1.75	86	0.77	0.01800	0.9	0.1227	4.2	0.0495	4.1	0.00599	1.8	114.9	1.1	103.3	7.3	111	0.73	1.8	114.9	2.3	9.28	734
RNZ87-06	c	1.63	78	0.76	0.01850	1.0	0.1225	3.9	0.0480	3.7	0.00586	1.8	118.5	1.2	116.2	6.5	102	0.06	1.7	118.5	2.4	9.18	734
RNZ87-07	c	2.45	110	1.13	0.01812	0.8	0.1235	3.5	0.0494	3.4	0.00570	1.3	116.9	1.0	119.3	7.1	98	−0.05	1.8	116.9	2.3	16.70	788
RNZ87-08	r	1.76	92	0.49	0.01805	0.8	0.1447	4.4	0.0581	4.4	0.00656	2.5	114.4	1.0	112.2	7.8	102	1.29	5.0	114.4	2.3	4.55	676
RNZ87-09	c	2.25	105	1.00	0.01795	0.6	0.1265	3.6	0.0511	3.5	0.00584	1.6	115.1	0.8	111.4	8.1	103	0.49	1.1	115.1	2.2	12.12	758
RNZ87-10	r	1.38	69	0.75	0.01787	0.9	0.1108	4.2	0.0450	4.1	0.00568	1.8	114.7	1.1	104.4	6.7	110	0.12	1.7	114.7	2.4	12.63	762
RNZ87-11	r	2.47	120	0.74	0.01828	0.7	0.1420	2.9	0.0564	2.8	0.00629	1.7	116.1	0.9	111.5	7.5	104	1.19	1.7	116.1	2.3	5.57	692
RNZ87-12	c	1.60	71	1.10	0.01839	1.1	0.1590	3.6	0.0627	3.5	0.00657	1.7	115.6	1.4	97.6	11.0	119	2.65	1.6	115.6	2.5	10.06	742

* radiogenic component only; *bd*l below detection limit; *r* rim, *c* core; concordance based on agreement between 206Pb*/238U-207Pb*/235U ages

Table 2 U-Th-Pb isotope and Ti concentration data for zircons from Separation Point granitoids and Western Fiordland Orthogneiss (Fiordland)

Analysis	Domain	Pb* (ppm)	U (ppm)	Atomic Th/U	Measured isotope ratios and 1 s (%) internal errors								Corrected ages (Ma) and absolute internal errors (1 s)							Selected age (Ma)	±	Ti (ppm)	*T* (°C)
					206Pb/ 238U	±	207Pb/ 235U	±	207Pb/ 206Pb	±	208Pb/ 232Th	±	206Pb*/ 238U	±	207Pb*/ 235U	±	Concord-ance (%)	Common 206Pb (%)	Spot MSWD				
North Fiord Granite																							
NF3-01	c	2.09	95	0.86	0.01918	0.8	0.1407	3.7	0.0532	3.6	0.00610	1.4	**123.2**	1.0	132.2	7.6	93	0.07	1.6	123.2	2.5	3.28	652
NF3-02	r	3.53	149	1.12	0.01920	0.7	0.1394	2.7	0.0527	2.7	0.00637	1.4	**123.0**	1.3	119.5	16.3	103	0.63	2.1	123.0	2.6	2.30	626
NF3-03	c	8.10	334	1.07	0.01994	0.7	0.1354	1.9	0.0493	1.8	0.00639	1.2	**128.2**	1.2	126.1	13.7	102	0.13	4.2	128.2	2.6	2.71	638
NF3-04	c	6.38	275	1.04	0.01933	0.4	0.1305	1.9	0.0490	1.9	0.00612	0.9	**124.4**	0.8	124.2	10.1	100	0.02	1.8	124.4	2.4	bdl	
NF3-05	c	3.19	148	0.57	0.02005	0.7	0.1344	2.8	0.0486	2.7	0.00646	1.7	**128.2**	1.0	122.7	7.6	105	0.25	1.8	128.2	2.5	bdl	
NF3-06	r	10.17	522	0.50	0.01854	0.6	0.1277	1.4	0.0500	1.2	0.00595	1.0	**118.9**	0.8	121.2	3.3	98	0.04	4.6	118.9	2.3	2.80	640
NF3-07	c	8.67	381	0.90	0.01956	0.4	0.1344	1.9	0.0498	1.9	0.00615	0.8	**125.9**	0.6	130.3	4.0	97	−0.11	2.5	125.9	2.3	3.09	647
NF3-08	r	18.48	868	0.68	0.01935	0.4	0.1311	1.2	0.0491	1.1	0.00615	0.8	**124.2**	0.5	124.7	3.2	100	0.02	3.4	124.2	2.3	3.27	651
NF3-09	c	4.02	177	0.91	0.01936	0.7	0.1314	2.6	0.0492	2.5	0.00640	1.2	**123.6**	1.0	109.7	7.4	113	0.75	2.4	123.6	2.4	2.78	640
NF3-10	r	30.23	1671	0.44	0.01742	0.7	0.1221	1.2	0.0508	1.0	0.00594	0.9	**111.1**	0.8	106.6	2.3	104	0.55	22			3.66	660
NF3-11	r	15.04	665	1.09	0.01846	0.7	0.1269	1.3	0.0498	1.1	0.00610	0.9	**118.1**	0.9	105.7	6.6	112	0.78	6.8	118.1	2.3	bdl	
NF3-12	c	11.25	286	0.86	0.03464	1.0	0.2454	1.7	0.0514	1.4	0.01004	2.2	**223.6**	2.4	245.7	19.4	91	−0.68	8.9			4.06	668
NF3-13	r	5.77	280	0.69	0.01867	0.7	0.1262	2.2	0.0490	2.1	0.00593	1.1	**119.9**	0.9	120.3	5.2	100	0.02	3.4	119.9	2.3	bdl	
NF3-14	c	0.84	38	0.49	0.02032	1.5	0.3123	4.6	0.1115	4.3	0.01283	3.2	**120.4**	2.0	112.9	17.2	107	8.04	1.6	120.4	2.9	bdl	
NF3-15	r	5.94	294	0.64	0.01841	0.8	0.1373	1.7	0.0541	1.5	0.00626	1.2	**118.7**	1.0	118.5	8.5	100	0.62	3.2	118.7	2.4	bdl	
NF3-16	c	3.52	166	0.96	0.01801	0.5	0.1252	2.9	0.0504	2.8	0.00585	1.2	**115.5**	0.8	111.3	9.1	104	0.44	1.3	115.5	2.2	3.33	653
NF3-17	r	16.33	568	1.76	0.02065	0.7	0.1670	1.9	0.0587	1.8	0.00633	0.8	**135.5**	1.8	182.5	24.1	74	−1.21	8.5			4.91	682
NF3-18	c	2.75	134	0.62	0.01880	0.8	0.1263	3.2	0.0487	3.1	0.00655	2.5	**119.7**	1.0	104.1	8.8	115	0.82	1.6	119.7	2.4	2.62	635
NF3-19	r	11.90	618	0.78	0.01704	0.6	0.1222	2.2	0.0520	2.1	0.00552	0.9	**109.4**	0.7	111.7	3.6	98	0.29	2.7			3.11	648
NF3-20	c	29.85	895	3.96	0.01655	0.8	0.1322	1.6	0.0579	1.4	0.00487	0.9	**122.7**	4.8	290.5	57.7	42	−10.09	32		4.8	12.60	762
NF3-21	r	16.88	744	1.05	0.01894	0.9	0.1448	2.1	0.0555	1.9	0.00579	1.5	**122.9**	1.2	152.8	6.0	80	−0.78	5.8	122.9	2.5	bdl	
NF3-22	c	2.64	127	0.57	0.01925	0.9	0.1476	3.0	0.0556	2.8	0.00691	2.7	**121.8**	1.2	110.9	9.2	110	1.40	1.7	121.8	2.5	bdl	
NF3-23	r	14.81	758	0.85	0.01708	0.5	0.1198	1.5	0.0509	1.4	0.00530	0.9	**110.3**	0.6	120.1	3.4	92	−0.29	3.0			4.02	667
Takahe Granodiorite																							
SF2a-01	c	3.91	155	0.47	0.02406	1.4	0.1649	4.7	0.0497	4.5	0.00851	2.7	**152.6**	2.2	131.9	9.2	116	0.91	3.9			3.38	654
SF2a-02	r	4.57	234	0.51	0.01850	0.6	0.1372	2.3	0.0538	2.2	0.00634	1.3	**117.8**	0.8	116.7	5.3	101	0.70	2.1	117.8	2.3	3.16	649
SF2a-03	c	11.98	564	0.64	0.01950	0.4	0.1287	1.6	0.0479	1.5	0.00611	0.7	**125.3**	0.6	125.9	3.1	99	−0.14	2.7	125.3	2.3	5.72	694
SF2a-04	r	23.44	1248	0.35	0.01866	0.7	0.1273	1.4	0.0495	1.2	0.00569	1.4	**119.8**	0.8	126.8	2.8	94	−0.26	10	119.8	2.3	3.15	649
SF2a-05	c	2.03	86	0.49	0.02249	1.3	0.1546	5.3	0.0499	5.1	0.00732	2.4	**143.5**	1.9	139.7	8.8	103	0.27	1.9			6.59	706
SF2a-06	r	10.71	484	0.77	0.01960	0.7	0.1317	1.5	0.0487	1.4	0.00628	1.1	**125.7**	1.0	122.0	5.5	103	0.17	5.9	125.7	2.5	2.50	632
SF2a-07	c	4.65	189	0.41	0.02395	0.7	0.1595	3.5	0.0483	3.4	0.00813	1.8	**152.4**	1.1	138.6	6.4	110	0.46	1.9			3.23	651
SF2a-08	r	5.25	261	0.36	0.01975	0.6	0.1508	2.5	0.0554	2.4	0.00728	1.6	**125.2**	0.8	122.6	4.1	102	0.96	5.0	125.2	2.4	bdl	
SF2a-09	c	7.65	312	0.73	0.02202	0.5	0.1544	1.7	0.0508	1.6	0.00699	1.2	**141.3**	0.9	146.9	7.3	96	−0.05	2.5			3.50	656
SF2a-10	r	8.66	386	0.88	0.01941	0.5	0.1350	1.6	0.0505	1.6	0.00609	0.9	**124.9**	0.7	131.3	5.3	95	−0.13	2.9	124.9	2.4	2.98	645
SF2a-11	r	9.21	312	0.94	0.02474	0.9	0.2128	2.3	0.0624	2.1	0.00934	1.7	**154.0**	1.5	114.5	8.5	135	3.16	7.2			5.09	685
SF2a-12	c	17.81	734	0.92	0.02076	0.6	0.1671	1.6	0.0583	1.5	0.00681	1.0	**132.8**	0.9	146.1	6.9	91	0.50	6.4		2.5	3.86	664
SF2a-13	r	23.09	798	2.17	0.01914	0.5	0.1317	1.2	0.0499	1.1	0.00578	0.8	**127.7**	1.0	174.7	11.9	73	−2.45	6.5	127.7	2.5	4214	1857
SF2a-14	r	4.97	242	0.37	0.02006	0.7	0.1784	2.6	0.0645	2.5	0.00807	1.9	**126.5**	0.9	134.9	6.6	94	1.52	1.7	126.5	2.5	bdl	
SF2a-15	r	22.26	878	1.78	0.01815	0.7	0.1295	1.5	0.0517	1.3	0.00537	1.0	**120.6**	1.2	171.5	11.7	70	−2.52	12	120.6	2.5	6.41	703

Table 2 continued

Analysis	Domain	Pb* (ppm)	U (ppm)	Atomic Th/U	Measured isotope ratios and 1 s (%) internal errors								Corrected ages (Ma) and absolute internal errors (1 s)							Selected age (Ma)	±	Ti (ppm)	*T* (°C)
					206Pb/ 238U	±	207Pb/ 235U	±	207Pb/ 206Pb	±	208Pb/ 232Th	±	206Pb*/ 238U	±	207Pb*/ 235U	±	Concord- ance (%)	Common 206Pb (%)	Spot MSWD				
SF2a-16	r	50.20	2529	0.41	0.01884	0.5	0.2894	1.4	0.1114	1.3	0.01137	1.2	**113.9**	0.6	147.1	5.0	77	5.94	15		2.2	49.89	905
SF2a-17	r	1.80	97	0.39	0.01798	0.8	0.1572	3.5	0.0634	3.5	0.00698	2.4	**113.6**	0.9	121.3	5.9	94	1.42	1.3		2.2	bdl	
SF2a-18	r	6.85	348	0.51	0.01870	1.0	0.1323	3.6	0.0513	3.5	0.00601	1.7	**119.7**	1.2	122.6	6.0	98	0.18	2.7	119.7	2.5	3.96	666
SF2a-19	c	6.66	352	0.47	0.01818	0.4	0.1224	1.8	0.0488	1.8	0.00571	1.2	**116.6**	0.5	118.6	2.8	98	−0.07	1.5	116.6	2.2	bdl	
SF2a-20	r	6.74	320	0.61	0.01919	0.9	0.1814	4.0	0.0686	4.0	0.00752	5.2	**120.7**	1.1	129.7	10.1	93	1.97	3.4	120.7	2.5	4.39	674
Titiroa Granite																							
TT6-01	c	2.28	99	1.10	0.01884	0.9	0.1437	3.4	0.0553	3.3	0.00615	1.6	**121.4**	1.3	124.2	14.6	98	0.60	2.9	121.4	2.8	3.59	658
TT6-02	r	5.14	242	0.32	0.01748	1.4	0.4214	6.4	0.1748	6.2	0.03339	12.3	**94.3**	1.9	62.8	35.1	150	17.19	39			7.41	715
TT6-03	c	3.63	160	0.90	0.01946	1.3	0.1295	2.8	0.0483	2.5	0.00628	1.6	**125.8**	1.8	116.7	15.1	108	0.33	7.1	125.8	3.2	5.10	685
TT6-04	r	15.83	788	1.06	0.01666	1.6	0.1163	1.9	0.0506	1.1	0.00515	1.3	**109.4**	2.7	127.3	34.5	86	−0.87	42			9.08	733
TT6-05	c	17.95	743	0.72	0.02147	0.7	0.1472	1.2	0.0497	1.0	0.00769	1.4	**136.6**	1.0	103.1	5.8	132	1.57	10			6.36	703
TT6-06	r	26.83	1168	0.60	0.02074	1.0	0.2381	6.6	0.0832	6.6	0.00956	3.0	**128.5**	2.1	125.4	31.2	102	4.31	41	128.5	3.4	9.37	735
TT6-07	c	6.52	307	0.44	0.02041	1.2	0.1359	1.9	0.0483	1.5	0.00695	1.5	**130.6**	1.7	121.7	10.6	107	0.35	16	130.6	3.2	4.34	673
TT6-08	r	18.91	775	1.33	0.01899	1.4	0.5199	2.7	0.1986	2.3	0.01100	1.9	**101.3**	1.6	44.3	21.2	229	21.03	22			29.63	846
TT6-09	c	3.04	136	0.89	0.01916	0.9	0.1467	2.8	0.0555	2.6	0.00648	3.5	**122.9**	1.4	119.0	17.1	103	0.98	2.2	122.9	2.9	2.39	629
TT6-10	r	24.95	1389	0.39	0.01594	1.1	0.3802	3.9	0.1729	3.8	0.02001	6.8	**86.8**	1.1	54.0	16.5	161	17.17	33			21.36	812
TT6-11	c	3.99	195	0.73	0.01840	1.9	0.1334	3.9	0.0526	3.4	0.00592	2.6	**119.1**	2.3	122.9	10.3	97	0.22	7.2	119.1	3.4	4.58	677
TT6-12	c	8.29	421	0.78	0.01743	1.3	0.1276	2.9	0.0531	2.6	0.00568	1.4	**112.6**	1.8	113.1	19.9	99	0.47	11	112.6	2.9	3.89	664
TT6-13	r	32.39	1553	1.12	0.01713	1.9	0.1237	2.9	0.0523	2.2	0.00519	3.9	**113.3**	2.9	139.1	32.7	81	−1.13	19	113.3	3.7	12.12	758
TT6-14	c	3.76	163	1.20	0.01850	1.1	0.1465	3.5	0.0574	3.4	0.00613	1.5	**119.9**	1.9	116.1	26.6	103	1.15	4.4	119.9	3.1	7.03	711
TT6-15	r	19.63	849	0.94	0.01972	1.0	0.1471	3.7	0.0541	3.5	0.00630	1.0	**127.8**	1.4	137.0	9.7	93	0.11	21	127.8	3.0	6.48	704
TT6-16	c	2.47	113	0.89	0.01883	1.0	0.1354	3.1	0.0521	2.9	0.00597	1.7	**121.7**	1.5	129.6	14.0	94	−0.03	3.6	121.7	2.9	1.84	611
TT6-17	r	7.42	337	0.98	0.01857	1.0	0.1348	2.7	0.0527	2.5	0.00600	1.6	**119.9**	1.8	124.0	23.2	97	0.22	4.2	119.9	3.0	5.53	691
TT6-18	r	4.73	208	0.59	0.02044	1.1	0.2797	5.4	0.0993	5.2	0.01092	4.7	**124.1**	1.8	122.1	22.0	102	6.24	4.4	124.1	3.1	9.67	738
TT6-19	c	2.59	116	0.94	0.01888	0.9	0.1486	3.8	0.0571	3.7	0.00656	1.7	**120.7**	1.2	108.0	8.8	112	1.62	2.5	120.7	2.7	2.56	634
TT6-20	c	3.76	162	1.25	0.01841	0.8	0.1255	2.6	0.0494	2.4	0.00591	1.2	**119.9**	1.0	113.1	8.2	106	0.35	3.1	119.9	2.7	3.17	649
TT6-21	r	19.92	1240	0.19	0.01662	0.8	0.1134	1.5	0.0495	1.3	0.00627	2.6	**106.0**	0.8	98.8	2.9	107	0.56	7.7			1.99	617
Western Fiordland Orthogneiss																							
WF01-01	c	4.45	180	1.32	0.01929	0.6	0.1330	2.2	0.0500	2.1	0.00611	0.9	**124.5**	0.8	126.4	5.5	98	0.02	2.2	124.5	2.4	27.51	838
WF01-02	r	3.27	136	1.36	0.01873	0.7	0.1276	2.8	0.0494	2.7	0.00576	1.1	**121.8**	0.9	135.9	7.3	90	−0.70	2.1	121.8	2.4	26.86	836
WF01-03	c	2.87	121	1.11	0.01953	0.7	0.1453	2.8	0.0540	2.7	0.00619	1.2	**125.7**	1.0	136.9	7.7	92	0.04	1.9	125.7	2.5	16.83	789
WF01-04	r	3.05	132	1.24	0.01832	0.7	0.1334	3.1	0.0528	3.0	0.00594	0.9	**117.6**	0.9	116.9	9.1	101	0.52	1.8	117.6	0.9	20.58	809
WF01-05	c	6.74	266	1.47	0.01916	0.6	0.1325	1.9	0.0501	1.8	0.00600	0.9	**124.2**	1.0	132.4	11.7	94	−0.30	3.0	124.2	2.5	19.94	806
WF01-06	r	6.33	252	1.37	0.01932	0.7	0.1310	2.4	0.0492	2.3	0.00619	0.8	**124.5**	1.2	120.3	14.9	103	0.23	3.7	124.5	2.6	26.96	836
WF01-07	r	2.06	86	1.11	0.01962	0.7	0.1318	3.8	0.0487	3.7	0.00611	1.6	**126.7**	1.0	131.8	8.2	96	−0.29	1.7	126.7	2.5	21.86	815
WF01-08	c	3.38	138	1.28	0.01929	0.7	0.1291	3.0	0.0486	3.0	0.00611	1.1	**124.3**	0.9	121.9	7.7	102	0.07	2.2	124.3	2.4	31.18	852
WF01-09	c	7.36	289	1.54	0.01897	0.5	0.1310	2.0	0.0501	1.9	0.00590	0.7	**123.3**	0.7	135.7	6.2	91	−0.53	2.5	123.3	2.3	29.24	845
WF01-10	r	3.34	140	1.25	0.01887	0.8	0.1424	2.8	0.0547	2.7	0.00614	0.9	**120.9**	1.0	120.7	6.5	100	0.72	2.7	120.9	2.4	22.01	815
WF01-11	c	1.71	77	0.75	0.01964	0.8	0.1278	3.6	0.0472	3.5	0.00641	1.5	**125.6**	1.1	112.6	6.3	111	0.45	1.4	125.6	2.5	14.80	777
WF01-12	r	4.52	189	1.15	0.01947	1.1	0.1774	2.7	0.0661	2.4	0.00622	1.4	**125.0**	1.5	158.1	6.9	79	0.39	5.0	125.0	2.7	14.06	772

Table 2 continued

Analysis	Domain	Pb* (ppm)	U (ppm)	Atomic Th/U	Measured isotope ratios and 1 s (%) internal errors								Corrected ages (Ma) and absolute internal errors (1 s)							Selected age (Ma)	±	Ti (ppm)	*T* (°C)
					206Pb/ 238U	±	207Pb/ 235U	±	207Pb/ 206Pb	±	208Pb/ 232Th	±	206Pb*/ 238U	±	207Pb*/ 235U	±	Concord-ance (%)	Common 206Pb (%)	Spot MSWD				
WF01-13	r	3.97	173	0.82	0.02010	1.4	0.1898	3.3	0.0685	3.0	0.00677	2.5	**128.0**	1.8	159.2	7.4	80	0.83	4.4	128.0	2.9	10.56	746
WF01-14	c	2.33	99	1.19	0.01888	0.8	0.1227	3.3	0.0471	3.2	0.00601	1.3	**121.9**	1.0	117.6	8.1	104	0.00	1.9	121.9	2.4	22.44	817
WF01-15	c	1.71	79	0.75	0.01933	0.9	0.1278	3.6	0.0479	3.5	0.00600	1.5	**124.4**	1.1	126.6	5.7	98	−0.22	1.6	124.4	2.5	16.34	786
WF01-16	r	2.78	123	0.90	0.01958	1.3	0.1791	3.4	0.0664	3.1	0.00616	2.6	**125.9**	1.7	168.1	7.5	75	−0.04	5.0	125.9	2.8	11.55	754
WF01-17	r	4.30	181	1.16	0.01917	0.7	0.1362	3.0	0.0515	2.9	0.00630	1.3	**122.6**	0.9	112.1	7.7	109	0.85	5.0	122.6	2.4	13.89	771
WF01-18	c	3.01	122	1.31	0.01925	0.7	0.1342	3.1	0.0506	3.0	0.00620	1.0	**123.7**	0.9	117.9	7.1	105	0.48	1.6	123.7	2.4	19.84	805
WF01-19	r	2.85	117	1.33	0.01893	0.8	0.1448	3.0	0.0555	2.9	0.00608	1.1	**121.7**	1.1	127.7	8.1	95	0.48	2.4	121.7	2.5	16.61	788
WF01-20	r	2.07	100	0.97	0.01744	0.8	0.1249	2.9	0.0519	2.8	0.00566	1.3	**111.8**	0.9	110.4	6.0	101	0.48	1.8			15.53	781
WF01-21	c	2.95	128	1.17	0.01851	0.7	0.1168	3.2	0.0458	3.1	0.00591	1.1	**119.1**	0.9	107.3	7.0	111	0.24	2.1	119.1	2.3	17.97	795
WF01-22	r	2.05	91	0.82	0.01960	0.8	0.1385	4.1	0.0512	4.1	0.00678	2.8	**124.8**	1.1	112.6	10.5	111	0.91	1.5	124.8	2.5	16.21	785

* radiogenic component only; *bdl* below detection limit; *r* rim, *c* core; concordance based on agreement between 206Pb*/238U-207Pb*/235U ages

are devoid of inherited cores and are characterised by prominent oscillatory zoning. Some grains display growth zoning that is progressively less luminescent toward the margins. A few grains contain substantially older cores that are otherwise indistinct from enclosing inner rims. Irregular, perturbed oscillatory zoning in some grains may be ascribed to sub-solidus recrystallisation and corrosion. Mineral inclusions are minor. Most grains are rimmed by a fine, bright zone with a generally regular and sharp contact to the interior domains. Along the grain surface, this rim is generally less regular and locally embayed, probably due to corrosion.

Fifteen spot analyses (14 >90% concordant) were obtained with ^{206}Pb*/^{238}U dates ranging from 97 to 124 Ma. Three inherited cores have dates of 573 ± 12, 775 ± 43 and 1,016 ± 19 Ma. Interior domains and rims (excluding inherited cores and two anomalously young dates) combine to produce a weighted mean age of 112.1 ± 1.9 Ma (MSWD = 1.9, $N = 11$). When considered separately, interior and exterior zircon domains give indistinguishable mean ages of 112.1 ± 4.8 Ma (MSWD = 2.5, $N = 6$) and 110.1 ± 3.7 Ma (MSWD = 5.6, $N = 8$), respectively.

Pearse Granodiorite/central segment (RNZ83)

Zircons are large (~200–300 μm in length, aspect ratios ~1:3), subhedral to euhedral, mostly fragmented (probably due to sample processing) and short to long prismatic. Under CL, the grains are composed largely of homogeneous, moderately luminescent zircon, and inherited cores are absent. Oscillatory zoning is faint and delicate or lacking, and mineral inclusions are rare. Some grains exhibit a dark grey featureless interior that is enclosed by a finer, brighter, homogeneous rim. The interface between interior and exterior domains is sharp and regular to irregular, the latter feature suggesting some resorption. Other grains are composed of grey and homogeneous cores surrounded by finer rims of dark and bright zircon, with the contact varying between regular to irregular, again indicative of corrosion.

Eleven spot analyses (all >90% concordant) cover a range in ^{206}Pb*/^{238}U dates from 106 to 122 Ma, and no inherited cores were identified on the basis of significantly older dates. Three anomalously young dates (110, 110, 106 Ma) are interpreted to due to lead loss and are excluded from age calculations. The interior and exterior portions provide statistically indistinguishable ages of 118.2 ± 1.6 Ma (MSWD = 0.6, $N = 5$) and 119.4 ± 3.0 Ma (MSWD = 1.1, $N = 3$). Combining all analyses produces a weighted mean age of 118.6 ± 1.5 Ma (MSWD = 0.8, $N = 8$). This age is in excellent agreement

Fig. 3 Cathodoluminescence (*CL*) images of selected zircon crystals from eight studied granitoid samples. Many *grains* show truncated zoning and embayments indicative of resorption. *Circles* show location of analysed region by LA-ICPMS (U–Th–Pb, REE and Ti). Note that in most cases, core–rim age differences are significantly greater than analytical uncertainty. Grains are not shown at the same scale

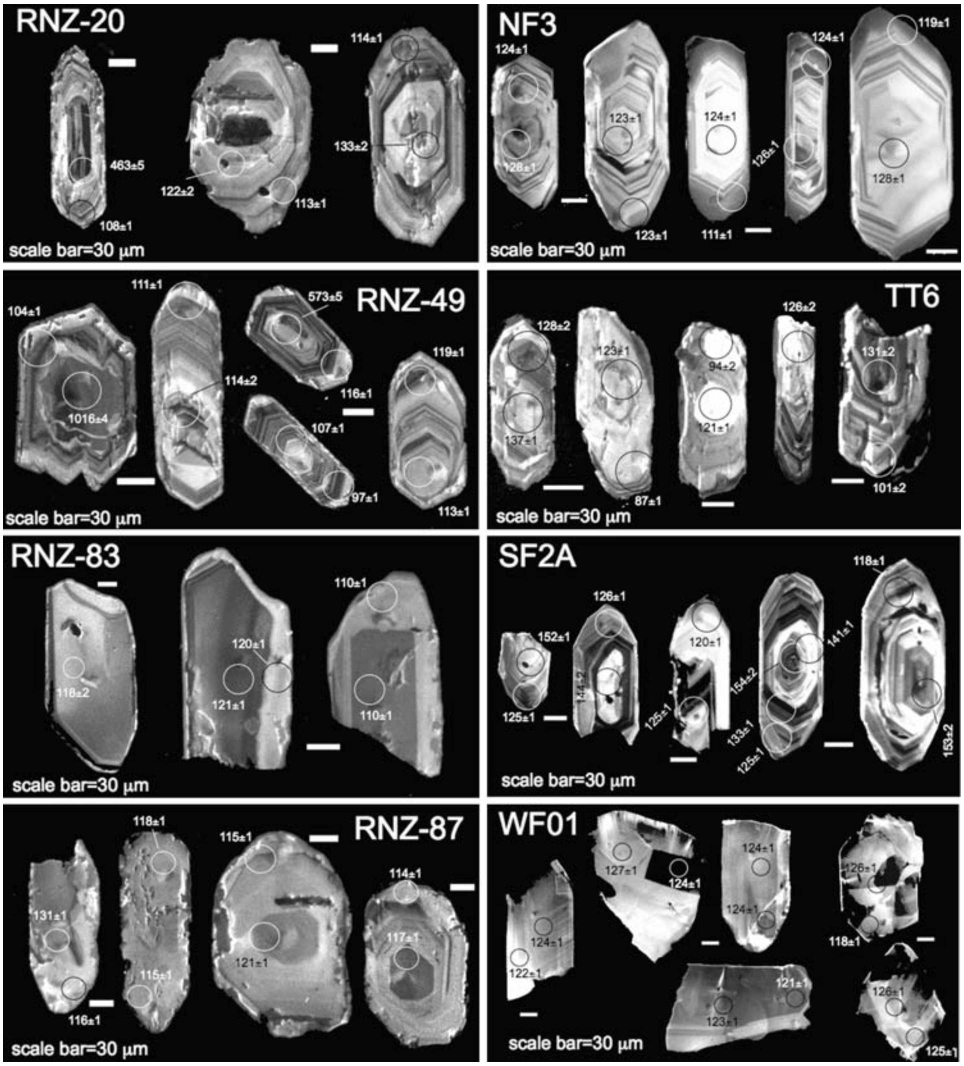

with the previous SHIRMP age of 119.4 ± 2.3 Ma for the same sample (Muir et al. 1994) and multigrain TIMS age of 117 ± 2 Ma for the unit (Kimbrough et al. 1994).

Rocky Granodiorite (RNZ87)

Zircons are euhedral, long prismatic or stubby to almost equant and range in length from ~150 to 250 µm (aspect ratios: 1:3 to 1:2). Internal structures are variable: some grains exhibit homogeneous to weakly growth-zoned interiors. Other grains display homogeneous, but irregular shaped interiors, possibly an indication for partial resorption prior to addition of new zircon material or solid-state recrystallisation. Some grains have darker interior domains compared with the enclosing material. These interior domains have boundaries parallel to oscillatory zoning and hence are not considered to be inherited cores. Corrosion is common along the contact between outer "cores" and marginal rims, which themselves are resorbed locally along the outer surface of grains. Distinct cores and mineral inclusions are absent. A significant role of corrosion or resorption is further indicated by the pitted surface of some grains.

Eleven spot analyses (ten >90% concordant) produce dates of 115–119 Ma, with one core being noticeably older (131 ± 3 Ma). Pooling 11 analyses produces an age of 115.9 ± 1.0 Ma (MSDW = 0.4, $N = 11$), while interior and exterior domains give ages of 117.0 ± 1.6 Ma (MSDW = 0.5, $N = 5$) and 115.1 ± 0.6 Ma (MSDW = 0.1, $N = 6$), respectively.

Eastern Fiordland

North Fiord granite (NF3)

Zircon grains are euhedral, prismatic, elongate to stubby and vary in length (~150–400 µm), with aspect ratios of 1:2 to 1:5. Under CL, the grains show simple internal

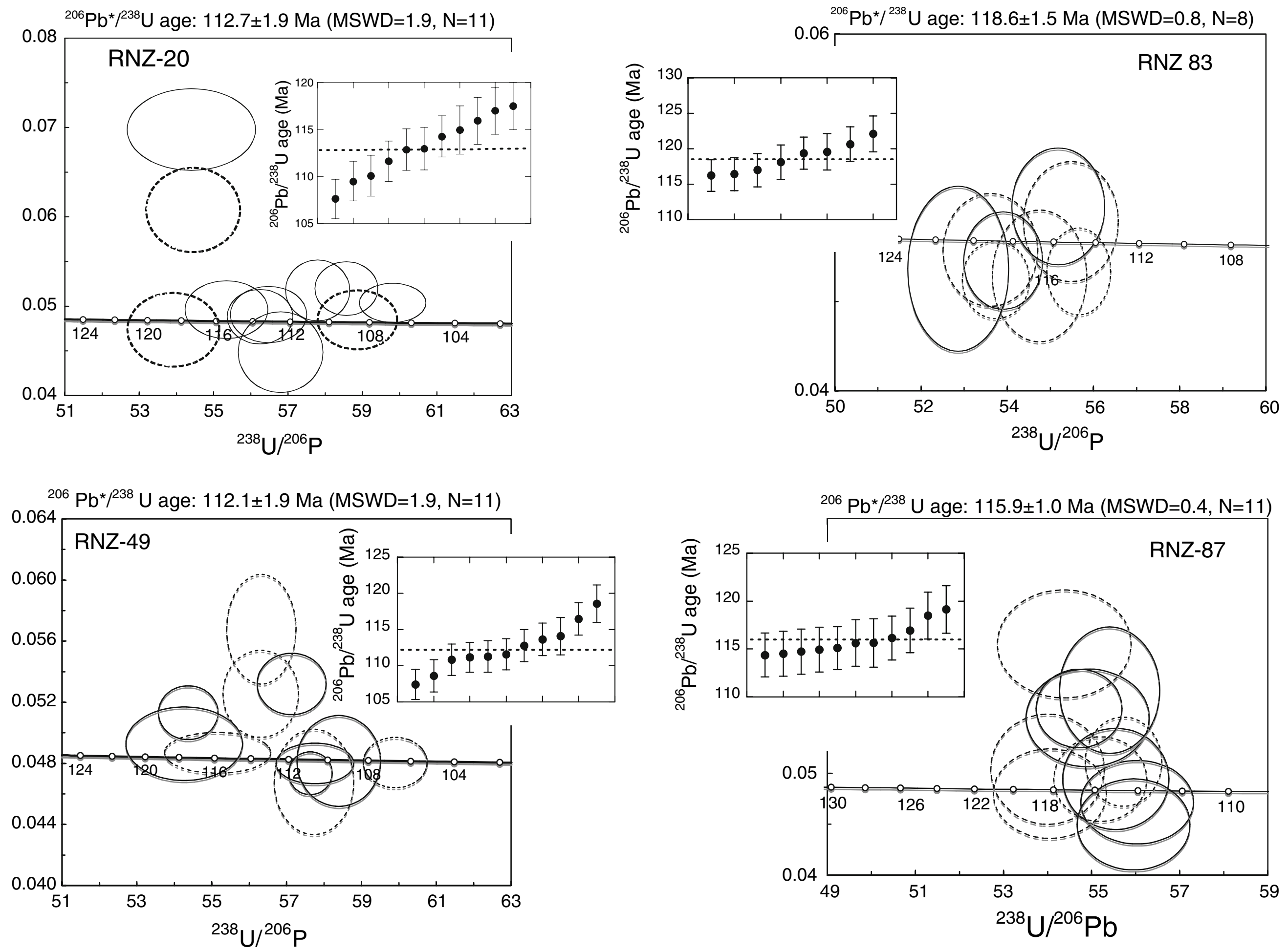

Fig. 4 Tera-Wasserburg concordia diagrams showing uncorrected (common Pb) U–Pb isotopic compositions of zircons extracted from eight granitoid samples. Cores are shown as *dashed ellipses*, rims as *continuous ellipses*. Data error point ellipses are 2σ. *Insets* show weighted mean and errors bars for individual spot analyses (1 SE) used for age calculation. Uncertainties on the pooled ages are reported at the 2 SE level. Only magmatic (i.e. no inherited) zircon ages are shown. Diagrams were generated using ISOPLOT version 3.00

features: with one exception, all grains lack inherited cores, and centres are commonly featureless and weakly luminescent. Oscillatory zoning is present in all grains and tends to become more pronounced towards the margin. Some grains display irregular, homogeneous patches with diffuse boundaries, which crosscut or obliterate growth-zoned domains, possibly related to subsolidus modification during late-magmatic stages.

Nineteen spot analyses (17 >90% concordant) define a range in ^{206}Pb*/^{238}U dates from 109 to 128 Ma. Two inherited cores give dates of 136 ± 2 and 224 ± 5 Ma. Cores and rims provide weighted averages of 123.0 ± 2.5 Ma ($MSWD = 2.7$, $N = 10$) and 117.7 ± 3.5 Ma ($MSWD = 5.9, N = 9$). When pooled spot analyses give an age of 122.0 ± 1.7 Ma ($MSWD = 2.2, N = 17$). Three spot analyses give dates of 109 ± 1, 110 ± 1 and 111 ± 1 Ma, which are significantly younger than the above calculated ages. These dates probably reflect lead loss, and hence were excluded from the age calculations. The pooled 122 Ma age is in good agreement with the previous SHIRIMP age of 123.7 ± 1.8 Ma for the sample (Muir et al. 1998) and multigrain TIMS age of 118 ± 3 Ma for the unit (Kimbrough et al. 1994).

Titiroa granite (TT6)

Zircon grains are mostly euhedral, long-prismatic and range in length from ~100 to 300 μm, with aspect ratios of 1:3 to 1:6. A small number of indistinct inherited cores were observed, and variably developed oscillatory zoning is the prominent structure in all grains. Luminescence is variable, but mostly moderate to weak. Mineral inclusions are lacking. Some grains exhibit marginal dissolution/resorption features (i.e. embayments). The polished surface of grains appears pitted and rough, which is attributed to sample processing.

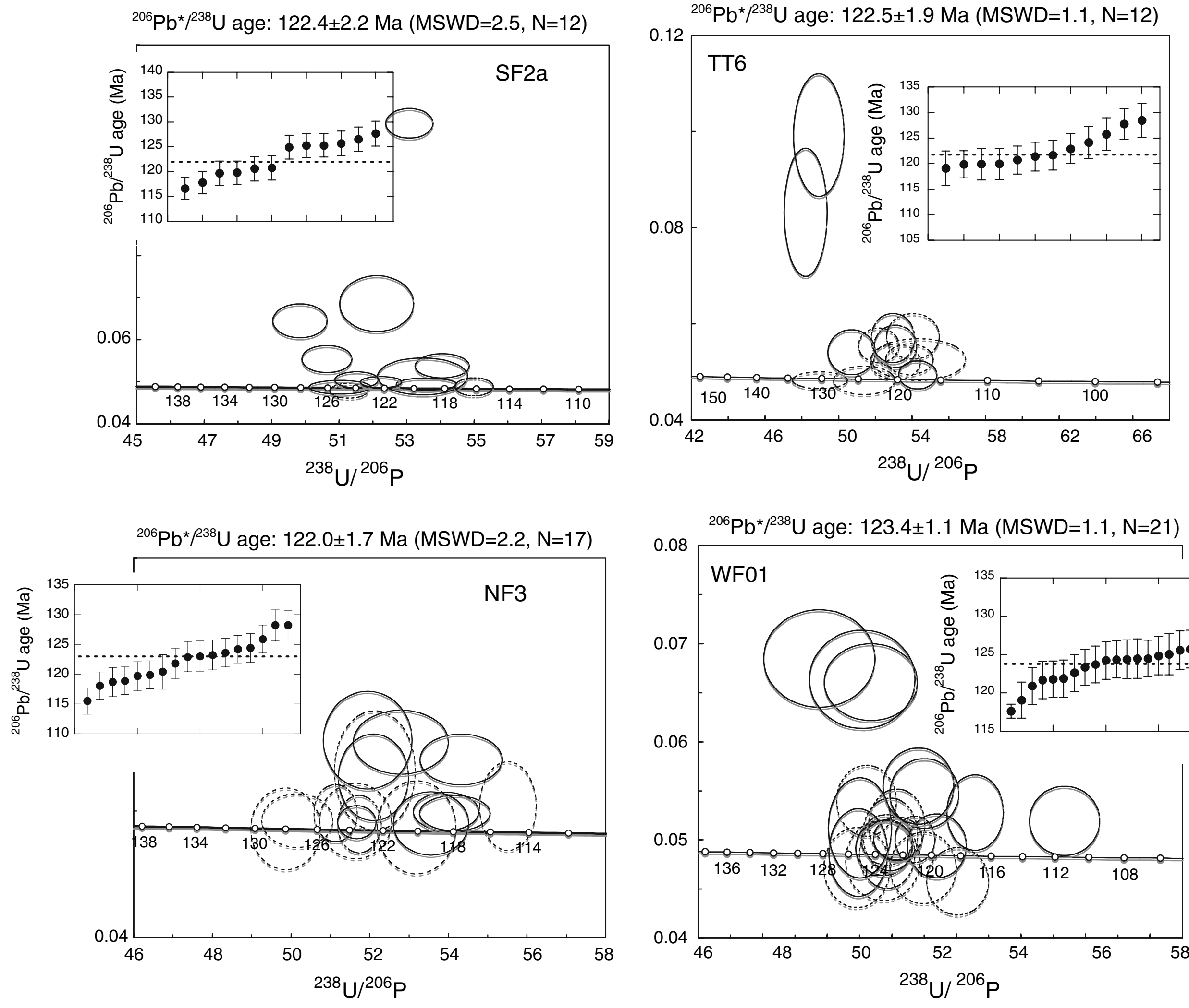

Fig. 4 continued

Nineteen spot analyses (14 >90% concordant) yield ^{206}Pb*/^{238}U dates of 87–129 Ma, with two inherited cores giving dates of 131 ± 2 and 137 ± 1 Ma. Six rims and one core appear substantially younger (<115 Ma) and may reflect Pb loss in view of their discordant nature; these dates were excluded from age calculations. Interior and exterior domains give weighted averages of 121.4 ± 1.5 Ma (MSWD = 0.5, $N = 8$) and 124.9 ± 3.9 Ma (MSWD = 1.6, $N = 4$), respectively, both ages being statistically indistinguishable from a pooled average of 122.5 ± 1.9 Ma (MSWD = 1.1, $N = 12$). The latter age is in excellent agreement with the SHRIMP age of 120.9 ± 1.8 Ma published by Muir et al. (1998).

Takahe Granodiorite (SF2a)

Zircons are euhedral, prismatic, elongate to stubby and relatively uniform in geometry, with lengths of ~100–300 μm and aspect ratios of 1:2 to 1:3. The internal makeup is complex, with some grains showing distinct core–rim relationships. Cores are sub-rounded, with subtle zoning and bright luminescence, and the contacts with growth-zoned inner rims are irregular to sharp. Homogeneous cores are also present. Most grains are characterised by well-developed oscillatory zoning in both cores and rims. Oscillatory zoning ranges from fine to broad and displays variable luminescence. Some grains display patchy to irregular replacement of growth zoning by compositionally uniform zircon with moderate luminescence. Mineral inclusions are rare. Resorption features are common and occur at core–rim or inner rim–outer rim contacts, or along the margin of grains, suggesting multiple resorption/dissolution events during the history of zircon growth.

Fourteen spot analyses (11 >90% concordant) span a range in ^{206}Pb*/^{238}U dates from 114 to 128 Ma, with six inherited cores giving substantially older dates of 133 ± 1, 141 ± 1, 144 ± 2, 152 ± 1, 153 ± 2 and 154 ± 2 Ma.

Interior domains (excluding inherited cores) and rims have weighted ages of 120.6 ± 8.6 Ma (MSWD = 7.4, $N = 2$) and 122.8 ± 2.2 Ma (MSWD = 2.1, $N = 10$), respectively. Combining all zircon domains (excluding inherited cores) yields an age of 122.4 ± 2.2 Ma (MSWD = 2.5, $N = 12$), which is identical within uncertainties to the SHRIMP age of 123.3 ± 1.8 Ma (Muir et al. 1998).

Western Fiordland Orthogneiss (WFO1)

Zircon grains are sub-to euhedral, angular to prismatic and mostly fragmented, probably due to damage during sample preparation. They vary in length (~150–250 μm) and have aspect ratios of 1:1 to 1:3. Under CL, zircons exhibit either irregular to patchy zoning, with fine oscillatory zoning being developed in fewer grains, or homogeneous and featureless cores. Inherited cores and mineral inclusions are lacking. Luminescence is variable and mostly weak. Some grains show a fine outer rim with bright luminescence. The contacts of these rims are sharp and mostly regular, although some zircons display resorption along their margins, suggesting dissolution and subsequent precipitation during the final stages of zircon growth. Fractures occur in some grains and appear healed by new zircon growth.

Twenty one spot analyses (17 >90% concordant) yield a range in $^{206}Pb^{*}/^{238}U$ dates from 118 to 128 Ma, with one date (112 Ma) probably representing Pb loss. When considered separately, cores and rims give identical weighted averages of 123.6 ± 1.2 Ma (MSWD = 0.7, $N = 10$) and 123.3 ± 1.8 Ma (MSWD = 1.4, $N = 11$), respectively. A pooled age of 123.4 ± 1.1 Ma (MSWD = 1.1, $N = 21$) is in good agreement with the previously reported SHIRIMP age of 125.9 ± 1.9 Ma (Muir et al. 1998).

Discussion

Geochronology

Comparison with previous studies using SIMS

U–Pb SHRIMP ages were previously determined by Muir et al. (1994, 1995, 1998) for six of the SPS/WFO plutons examined in this study. Figure 5 illustrates the good agreement between LA-ICPMS and SHRIMP ages. Excluding one ICPMS analysis (RNZ20), ages from both datasets yield a good correlation ($R = 0.9$). The precision of both ICPMS and SHRIMP U–Pb age data are comparable (ICMPS: 1–2.2 Ma vs. SHRIMP 1.8–2.3 Ma, 2σ).

Given differences inherent in SHRIMP and LA-ICPMS analysis, the agreement between both datasets for SPS/WFO plutons is remarkable. For instance, sample heterogeneity may be expected to account for less precise measurements by ICPMS, given the difference in sampled volume of zircon (2 ng for SHRIMP vs. up to 400 ng for LA-ICPMS: Kosler et al. 2002). Evidently, effects of sample heterogeneity are negligible in this study, presumably because of very similar U–Pb isotopic compositions of interior and exterior domains encountered in most SPS/WFO zircons. Distinctly variable U/Pb (and other elemental and isotopic ratios), when intersecting different zircon growth domains (albeit dependant on the size and geometry of the ablation pit), are usually easily detectable in the time-resolved ICPMS signal. Due to larger sampling volumes, LA-ICPMS is potentially less prone to surface contamination by common Pb. Conversely, the poor mass resolution of the ICP and ^{204}Hg background make measurement of ^{204}Pb very difficult.

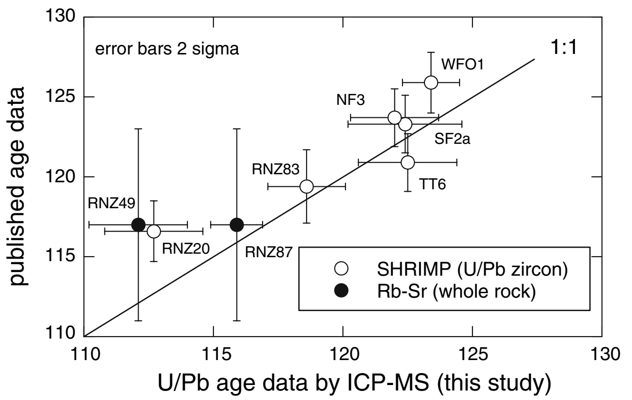

Fig. 5 Comparison between published zircon SHRIMP (pooled) and Rb–Sr whole rock age data (Muir et al. 1994, 1995, 1998) and zircon IC-PMS ages from this study. Note that both SHRIMP and IC-PMS ages have comparable levels of analytical precision (~1–2 myr at 2σ). Diagram was generated using ISOPLOT version 3.00

Inheritence

A small, but significant proportion of the zircons analysed by LA-ICPMS are inherited, in accord with previous studies by Muir et al. (1994, 1995, 1998). This is evident in a probability density plot of U–Pb ages (Fig. 6), which combines both SHRIMP and LA-ICPMS datasets. Zircon populations from SPS plutons (principally from the Separation Point Batholith in Nelson) are characterised by a lack of inherited grains with ages > 1,100 Ma, and minor age peaks at 500–600 and ~1,000 Ma. Age spectra with prominent peaks at 500–700, 900–1200 Ma and minor older peaks have been also reported from inherited zircon cores in Devonian granitoids of New Zealand (Muir et al. 1996) and metasedimentary enclaves in S-type granites from the Lachlan Fold Belt (Elburg 1996; Keay et al. 1999; Maas et al. 2001), and appear to be a characteristic feature

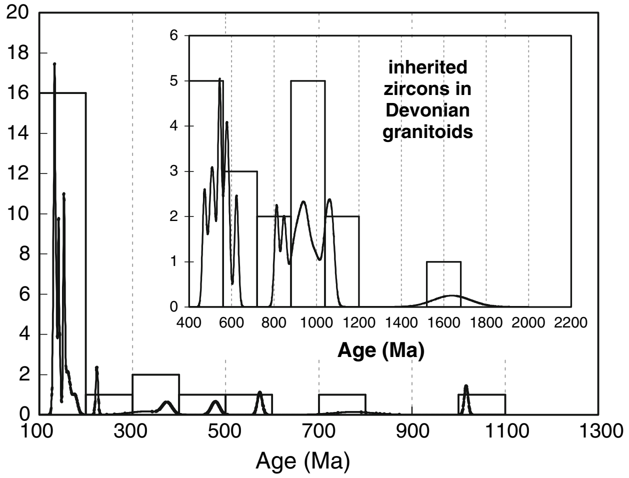

Fig. 6 Probability density diagram showing age distribution of zircons with dates >130 Ma. Diagram is based on U–Pb age data from this study and from Muir et al. (1994, 1995, 1998). Note subtle age peaks at ~1,050 and 500–600 Ma, characteristic of age spectra for inherited zircons in Paleozoic granites from New Zealand and the Lachlan Fold Belt, and detrital zircons in Ordovician sedimentary rocks in Australia and New Zealand. *Inset* diagram displaying inherited ages for zircons from Devonian granitoids (Muir et al. 1996). Diagram was generated using ISOPLOT version 3.00

of Palaeozoic sedimentary rocks from the eastern margin of Gondwana now preserved in Australia, New Zealand (Greenland Group metasediments) and Antarctica (Ireland 1992; Jongens et al. 2003; Muir et al. 1995, 1996; Williams et al. 1992; Wysoczanski et al. 1997). Similar age spectra were reported by Kemp et al. (2005a) from zircons within I-type granitoids from the Lachlan Fold Belt, which these workers considered as xenocrysts entrained from surrounding metasedimentary host rocks.

Importantly, the present LA-ICPMS and previous SHRIMP data identifiy a distinct age component at ~130–155 Ma (17 out of 237 zircons). This age range is clearly resolvable from inferred crystallisation ages of these Cretaceous granitoids (~112–124 Ma), and is therefore considered to represent inherited zircons. Mid-Jurassic to early Cretaceous putonic rocks in eastern Fiordland, collectively referred to as the Darran Suite, have been dated at 131–168 Ma (Kimbrough et al. 1994; Muir et al. 1998). Darran Suite granitoids can be regarded the most likely source for the 130–155 Ma zircons as first suggested by Muir et al. (1998). It is interesting to note that the sample of Takahe Granodiorite (SF2a) contains a relatively large fraction of inherited zircons (30% of all analysed grains) with ages of 133–154 Ma; this means that, while this rock clearly interacted with pre-existing crustal material, none contained zircons older than 155 Ma. Since Darran Suites plutons are also devoid of zircons >170 Ma (Muir et al. 1998), it is probable that Darran Suite material was the sole contributor of the inherited zircons. In the present study, Paleozoic and older zircon inheritance appears restricted to Nelson granites that intruded Takaka Terrane metasediments of lower Palaeozoic age, while Mesozoic inheritence is limited to eastern Fiordland granites that were emplaced into Mesozoic Darran Suite plutonics. This relationship strongly points towards emplacement-level contamination rather than source control. This conclusion accords with new zircon O and Hf isotope data (Bolhar et al. 2008), which show that SPS plutons were contaminated at emplacement level by heterogenous, local crust.

Compositional and thermal evolution

Zoning and core–rim textures of the studied zircons suggest variations in the composition and thermal condition of the plutonic systems during crystallisation. Textural and compositional zonation of accessory minerals have been previously employed in a number of studies to trace fundamental processes in igneous differentiation, such as magma mixing (Griffin et al. 2002), replenishment and melt extraction from crystal mush (Lowry-Clairborne 2007), resorption and recycling of rhyolite zircons (Miller and Wooden 2004) and accessory mineral saturation and fractionation in plutons (Evans and Hanson 1993; Hoskin and Black 2000; Wark and Miller 1993). In the present study, Th/U and Zr/Hf as two pairs of elements that are readily incorporated during zircon growth are used to track compositional changes in magmas that formed SPS/WFO plutons. Zircons have U and Th concentrations in the range of ~50–900 and ~20–800 pm, respectively, with corresponding Th/U ratios of 0.2–1.5 (Tables 1, 2). Th/U ratios tend to increase with increasing concentrations of U and Th. Given that U is four to five times more compatible in zircon than Th (Mahood and Hildreth 1983), the decrease of Th/U with increasing differentiation, as reflected by the decrease in crystallisation temperature (Fig. 7), requires another Th-rich accessory mineral, most probably monazite ([Ce, La, Th, Th]PO_4), as a fractionating phase to have lowered the Th/U of the SPS magmas.

In the four Nelson granitoids and WFO, Th/U display a monotonic, systematic decrease with decreasing *T*. Similar linear trends are also observed when Zr/Hf ratios are plotted against crystallisation temperature (Fig. 8). Recently, Lowery-Claiborne et al. (2007) have demonstrated the usefulness of Zr/Hf in zircon as monitor for magmatic fractionation in plutonic systems. Zircon concentrates both elements, but Zr is more strongly incorporated in zircon than Hf. As zircon crystallises and separates from the bulk magma, the residual melt becomes progressively depleted in Zr, resulting in subchondritic Zr/Hf in fractionated melt and zircon crystallising from it. It is notable that the best-defined trends in Zr/Hf versus *T* are

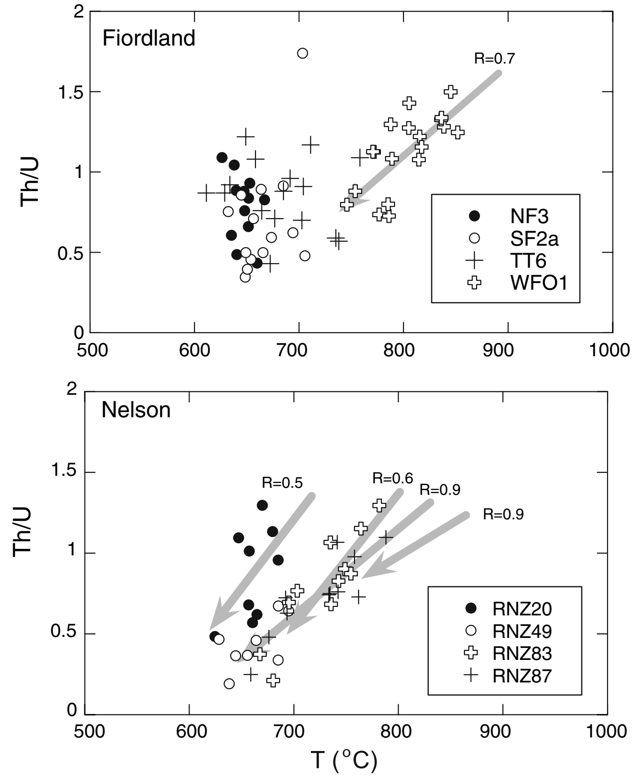

Fig. 7 Diagrams of Th/U versus crystallisation temperature for zircon (as determined using the Ti-in-zircon thermometer of Watson et al. (2006)) extracted from granitoids from Fiordland and Nelson. Well-defined linear correlations are indicated by *grey arrows* and correlation factors $R \geq 0.5$, suggesting a systematic change in melt composition as the system cooled. This trace element behaviour is consistent with simple differentiation processes, such as fractional crystallisation

recorded by zircons from most mafic samples RNZ83, 87 and WFO1. Those samples also preserve linear co-variations in Th/U versus temperature (Fig. 7). Thus, Th/U and Zr/Hf co-variability in three out of eight studied plutons suggests that magma differentiation followed a relatively simple fractional crystallisation path as those systems cooled. Notwithstanding these relatively coherent arrays, the range in elemental concentrations is inconsistent with a purely closed-system behaviour, as Th, U and, by interference, other incompatible elements would have varied by several orders of magnitude in the magma or crystal-melt mush, assuming K_D values remained insensitive to changes in PT conditions. Scatter about relatively well-defined regression lines may reflect localised compositional variability and disequilibrium due to saturation and growth of accessory and major minerals, which can drastically change trace element concentrations in isolated pockets of evolved melts trapped in the crystalline mush as they sequester trace metals (Wark and Miller 1993; Hoskin et al. 2000). For instance, certain elements with the highest mineral-melt partition coefficient would become relatively depleted in the melt in proximity to a particular precipitating mineral. Such observations accord with a growing body of evidence that granitoids represent a mix of cumulate and restitic minerals and batches of injected mafic melt injection, rather than a simple solidified melt (Wiebe 1993; Wiebe and Collins 1998).

The majority of analyses yield Th/U ratios of >0.5, especially of those zircons with the highest crystallisation temperatures (i.e. earliest stages in the crystallisation history). The range in Th/U values is significantly higher than values for mantle-derived zircon (Zartman and Richardson 2005), confirming previous studies that SPS/WFO magmas were substantially more evolved than primitive melts in equilibrium with peridotitic mantle.

Correlated zircon compositional data with $T_{\text{Ti-in-zircon}}$ are consistent with simple fractional crystallisation during magma cooling. If this simple scenario is valid for the majority of plutons, zircon Ti concentration data are expected to define a decreasing trend in crystallisation temperature from core to rim, consistent with the general direction of magma evolution towards cooler temperatures. This relationship can be explored by compiling calculated temperature differences between cores and their respective rims, expressed as δT [core–rim] in histograms of Fig. 9. Positive values denote a cooling trend from core to rim, whereas negative values indicate a “reverse trend”, with rims having formed at higher temperatures relative to the cores. One-half to two-thirds of all zircon core–rim pairs indicate progressive cooling from core to rim, with most grains suggesting a drop in temperature of <60°C from core to rim. This is consistent with progressive fractional crystallisation during cooling of zircon-saturated magmas. However, in both provinces (Nelson and Fiordland), there is also a substantial proportion of zircons, mostly from the most felsic samples, that document a reversed temperature trend from core to rim (~30–50%), with seven zircons suggesting an increase in ambient temperatures greater than 30°C during progressive crystallisation. The fact that the majority of zircon crystallised over a temperature range of <60°C may suggest temperature and compositional conditions of the system at the time of crystallisation, which were favourable for zircon nucleation and growth (i.e. eutectic-like conditions, presence of water to aid ion exchange). The mechanisms to account for temperature reversals in zircon cores and rims are probably related to replenishment of the magma reservoirs by injection of hot, more mafic melts or convective movement of thermally zoned magma or crystal mush, which would have exposed zircons to hotter and compositional less evolved melt. The former mechanism is given preference in view of generally high viscosities of silicic melts due to stronger polymerisation, in particular during later stages of the crystallisation history when the proportion of crystal mush to residual

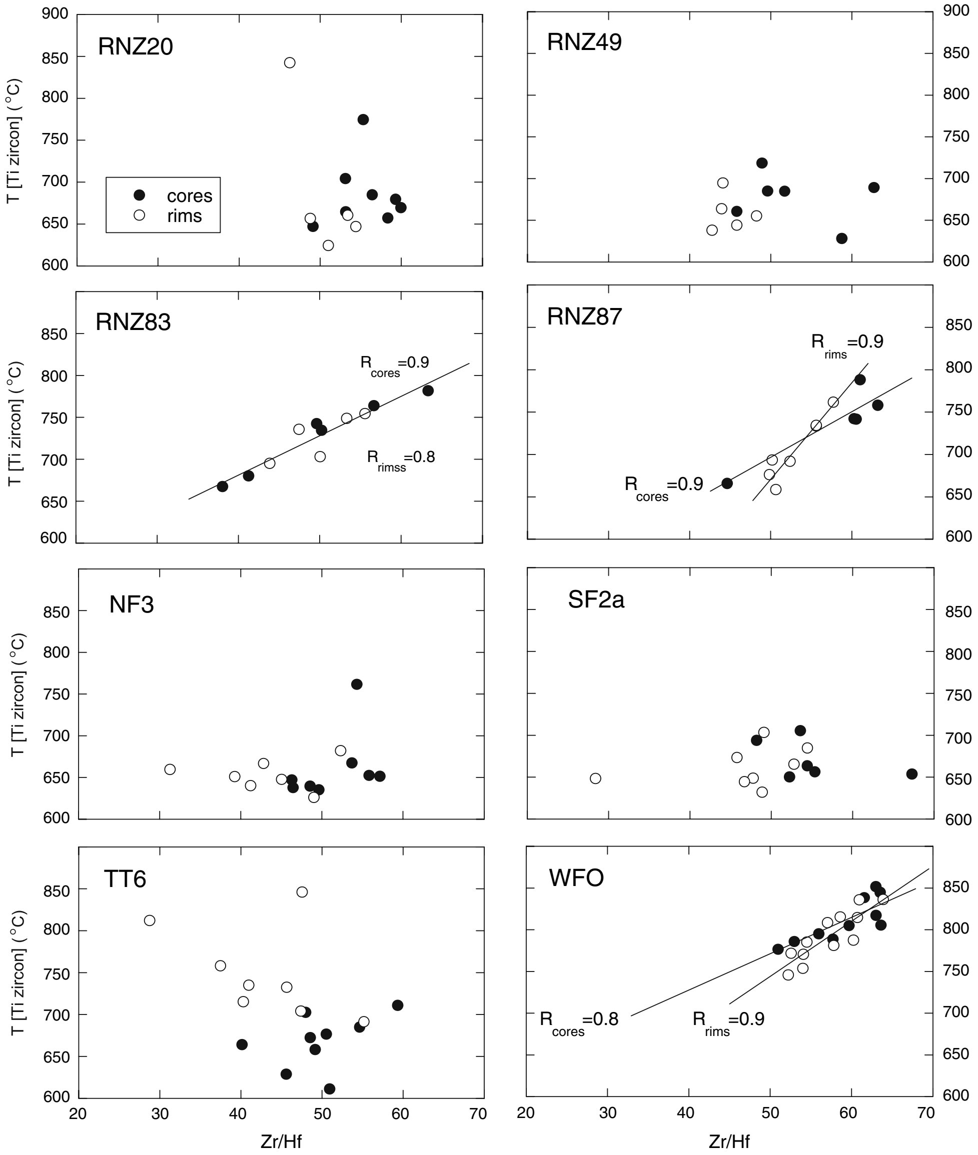

Fig. 8 Diagrams of crystallisation temperature versus zircon Zr/Hf. Linear trends are observed for zircons from RNZ83, RNZ87 and WFO1, with less well-defined trends for zircons from RNZ20 and RNZ49. The linear array points to fractional crystallisation of zircon, the main repository of Zr and Hf in plutonic rocks. Scatter in other datasets probably reflects open-system behaviour, such as zircon saturation in residual melt pockets or recharge by mafic magmas

melt would have been high. Importantly, zircons that sampled markedly different melts and crystallised under variable conditions were ultimately juxtaposed by some physical process(es) prior to magma solidification. Evidence from zircon compositions and thermometry for protracted assembly of plutonic systems, punctuated by repeated fractionation and reheating is in line with other studies (e.g. Lowery-Claiborne et al. 2007). In the present study, strong support for repeated reheating, possibly due to magma recharge, comes also from textural zoning in zircons indicative of resorption. Dissolution of zircon, as manifested by resorption features, was evidently related to changes from saturated to undersaturated conditions, which, in turn, are controlled by temperature, chemistry and the presence of aqueous fluids (Harrison and Watson 1983; Watson et al. 2006).

In the present study concomitant trends of decreasing Th/U and Zr/Hf with decreasing $T_{\text{Ti-in-zircon}}$ provide a clear record of evolving melt compositions in the most mafic samples (Figs. 7, 8). Observed trends are best explained in terms of monotonic cooling and fractionation of the magma–crystal mix, punctated by episodes of reheating/magma mixing and consequent resorption of zircon. In the most felsic samples, these correlations break down and zircon Th and U concentrations are highly variable, suggesting that zircons were in disequilibrium with each other and the melt (e.g. Miller and Wooden 2004). The simplest explanation may be that the mafic plutonic samples were protected from reworking (rejuvenation) by their higher melting point, possibly due to their cumulate nature, as reflected by simple Zr/Hf–Th/U–T trends. In contrast, the felsic plutonic samples were prone to rejuvenation by

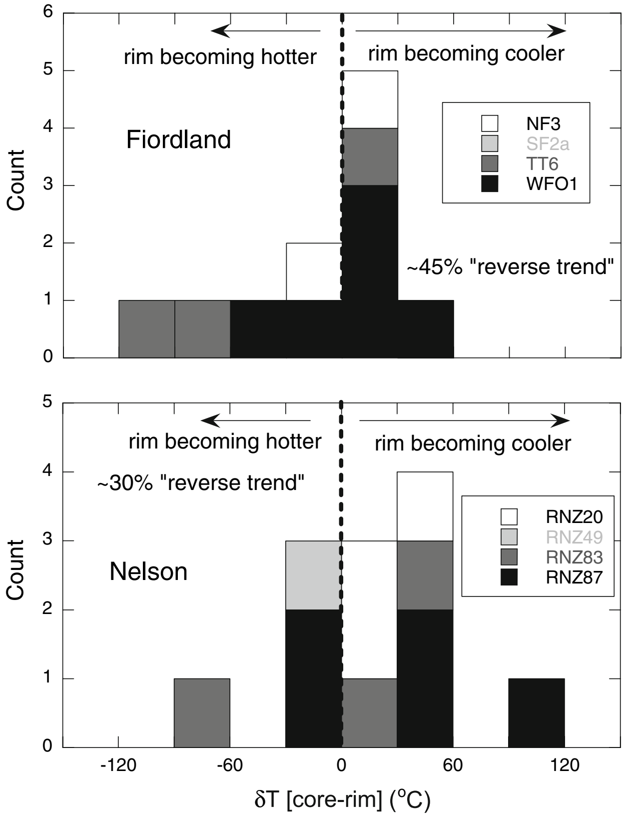

Fig. 9 Histograms showing calculated temperature differences between cores and rims within individual zircons. *Positive* and *negative* values denote a cooling and heating trend from core to rim, respectively. Note that 30–45% of zircons show a "reverse trend", suggesting that melt underwent fluctuations in temperature, possibly related to reheating due to input from mafic magmas

hotter, more mafic inputs due to their lower melting point (near eutectic). Finally, highly variable concentrations of Th and U in zircon from single granitoid samples, as demonstrated here, contrast markedly with generally uniform REE compositions in igneous zircon (Hoskin and Black 2000; Hoskin and Ireland 2000; Maas et al. 1992).

REE

Rare earth element data are reported in Table 3. As only La, Ce Sm, Eu, Dy and Lu were analysed by LA-ICPMS, the remaining REE were estimated through interpolation, using equations stated previously in "Analytical techniques". In chondrite-normalised Masuda-type diagrams (Fig. 2b), REE for averages calculated for cores and rims from all eight studied granitoids display compositions that are characteristic for terrestrial zircons (Hoskin and Schaltegger 2003): normalised patterns have steeply rising slopes from the light REE to the heavy REE ($\mathrm{Lu/Dy_{chond.}} \sim 5$–20), with pronounced positive Ce and negative Eu anomalies. This pattern geometry rules out post-solidus alteration and accidental analysis of undetected REE-rich mineral inclusions for most of the analysed zircons. However, a small number of spot analyses reveal enrichment in the LREE (e.g. RNZ20-07, RNZ87-11), which is positively correlated with P (Table 3). In these cases, elevated LREE probably reflect incidental incorporation of sub-surface mineral inclusions with enriched LREE, such as apatite, in the analysis volume (e.g. Cavosie et al. 2006). Apart from these anomalous analyses, REE concentrations are comparable to typical terrestrial zircon values (Hoskin and Schaltegger 2003). Salient REE features pertinent to the petrogenetic history of SP granites and WFO can be summarised as follows:

Average REE compositions calculated for cores and rims for individual granitoids are very similar, especially for granodiorite SF2a and orthogneiss WFO1, both in general shape and extent of Ce and Eu anomalies. The overall similarity of REE in zircon within all individual rocks is further highlighted by plots showing trace element compositions of single spot analyses: whereas REE concentrations vary by more than two orders of magnitude, the overall pattern shapes remain relatively unchanged. This observation suggests that changes in the evolving melt composition did not appreciably affect the REE systematics in crystallising zircon, in line with previous studies of granitic systems (Hoskin et al. 2000; Sawka 1988). Notwithstanding these general similarities, differences in REE compositions exist and are better appreciated in binary diagrams utilising zircon $\mathrm{Eu_{N}/Eu_{N}^{*}}$ and Ce(IV)/Ce(III) ratios. $\mathrm{Eu_{N}/Eu_{N}^{*}}$ ratios were calculated from chondrite-normalised concentrations as follows: $\mathrm{Eu_N/(Sm_N \times Gd_N)^{1/2}}$. Ce(IV)/Ce(III) ratios were calculated using a lattice strain model for mineral-melt partitioning (Blundy and Wood 1994), following the method outlined in Ballard et al. (2002). In diagrams of Ce(IV)/Ce(III) and $T_{\mathrm{(Ti\text{-}in\text{-}zircon)}}$ versus $\mathrm{Eu_{N}/Eu_{N}^{*}}$, single zircon spot analyses display considerable compositional variability, with Ce(IV)/Ce(III) and $\mathrm{Eu_{N}/Eu_{N}^{*}}$ values from 2 to 2,000 and from 0.2 to 1, respectively. The considerable variability in zircon trace element compositions is barely noticeable from normalised REE patterns, but is testimony to differentiation processes that affected the melt in which zircon became saturated. The nature of relative Eu and Ce variability in plutonic zircon and its petrogenetic significance is evaluated below:

Among the trivalent REE, which substitute for Zr in zircon, Eu and Ce are redox sensitive and therefore provide some information on the oxidation state of the crystallising medium. In normalised zircon REE patterns, the redox-controlled behaviour of both elements in plutonic environments is manifested in conspicuous positive Ce anomalies, as oxidised Ce(IV) is favoured over Ce(III), and

Table 3 LA-ICPMS trace element concentrations (in ppm) for zircons from Separation Point Suite granitoids

Domain	Sample	P	Y	*HfO$_2$* (wt%)	La	Ce	Sm	Eu	Dy	Lu
Separation Point Granite (N-segment)										
c	RNZ20-09	108.12	292.32	0.99	0.09	33.52	2.78	0.74	51.69	35.53
c	RNZ20-13	220.34	172.85	1.02	0.32	20.27	1.84	0.53	30.90	21.08
c	RNZ20-17	147.63	445.88	0.96	0.44	50.45	4.01	1.21	71.68	51.75
r	RNZ20-04	32.56	121.30	1.13	bdl	11.29	0.50	0.27	14.02	32.72
r	RNZ20-05	36.07	97.63	1.19	0.03	13.54	0.57	0.33	14.02	21.13
r	RNZ20-08	87.91	141.29	1.08	0.45	19.87	1.16	0.47	21.83	24.67
r	RNZ20-10	109.01	97.36	1.18	0.61	12.00	0.85	0.36	13.10	25.13
r	RNZ20-12	96.11	72.99	1.25	0.14	9.89	0.50	0.26	9.26	20.60
r	RNZ20-14	76.67	129.70	1.08	bdl	17.26	1.25	0.35	22.26	17.84
r	RNZ20-18	40.17	97.34	1.18	0.18	14.07	0.62	0.29	13.37	19.75
r	RNZ20-20	74.03	198.22	1.06	bdl	30.02	1.79	0.67	32.75	28.32
c	RNZ20-03*	78.87	146.90	1.09	0.11	18.45	1.43	0.36	25.94	19.69
c	RNZ20-06*	156.32	219.40	1.04	0.07	13.24	2.56	0.45	41.97	25.95
c	RNZ20-07*	645.05	432.28	0.98	6.63	44.41	8.48	2.30	85.52	38.58
c	RNZ20-11*	209.43	377.40	1.17	0.86	23.92	3.99	1.26	64.18	79.04
c	RNZ20-19*	247.55	940.45	1.09	4.98	31.19	15.64	0.94	193.72	68.99
Separation Point Granite (S-segment)										
c	RNZ49-04	186.22	769.28	1.42	bdl	54.27	3.25	0.74	113.27	97.63
c	RNZ49-07	556.20	1341.65	1.16	0.05	70.41	7.62	2.59	230.05	127.61
c	RNZ49-10	48.65	216.47	1.10	bdl	21.42	1.05	0.51	27.75	44.13
c	RNZ49-14	25.01	211.73	0.98	bdl	14.18	2.13	1.24	32.79	32.66
c	RNZ49-15	66.11	199.83	1.05	0.04	16.94	1.54	0.55	29.79	36.43
c	RNZ49-17	701.55	1438.92	1.12	bdl	27.59	4.09	1.25	222.85	148.81
r	RNZ49-03	553.91	1442.94	1.26	bdl	61.71	4.40	0.81	224.30	159.52
r	RNZ49-06	447.07	727.25	1.35	bdl	21.34	2.03	0.31	112.19	80.68
r	RNZ49-09	40.34	186.94	1.26	bdl	21.35	0.69	0.33	21.53	42.08
r	RNZ49-12	830.18	1689.77	1.19	bdl	44.26	4.94	1.07	266.53	159.97
r	RNZ49-13	178.62	297.27	1.33	bdl	9.39	0.78	0.28	43.23	44.87
r	RNZ49-16	449.79	722.76	1.32	bdl	18.92	1.90	0.33	110.47	78.13
r	RNZ49-18	784.01	1765.42	1.31	0.04	52.19	5.18	0.86	273.99	169.74
c	RNZ49-01*	202.36	1428.47	0.92	bdl	22.86	9.36	0.17	299.11	101.17
r	RNZ49-02*	308.38	621.84	1.34	0.11	14.45	1.26	0.26	90.35	79.32
c	RNZ49-05*	135.15	221.26	1.26	bdl	21.38	1.88	0.46	38.72	30.53
r	RNZ49-08*	1098.77	2381.35	1.31	0.11	75.84	9.78	1.69	407.17	199.22
c	RNZ49-11*	726.96	1137.84	1.18	0.13	33.08	5.64	1.22	190.48	112.35
Separation Point: Pearse Granodiorite										
c	RNZ83-01	94.39	203.56	1.16	0.03	11.29	2.09	0.37	38.31	23.59
c	RNZ83-03	126.29	415.37	1.15	bdl	18.19	5.17	0.79	81.54	40.17
c	RNZ83-07	81.65	123.88	1.51	bdl	10.54	0.60	0.09	19.28	20.96
c	RNZ83-10	201.00	700.43	0.91	0.09	17.20	10.25	1.70	134.61	60.41
c	RNZ83-11	138.41	429.93	1.02	0.04	14.57	7.23	1.20	86.89	38.12
r	RNZ83-04	103.95	428.52	1.31	bdl	23.55	4.12	0.63	76.93	54.50
r	RNZ83-08	104.20	274.27	1.08	bdl	13.85	3.02	0.52	50.91	30.17
r	RNZ83-12	161.01	274.27	1.04	bdl	14.75	3.66	0.60	53.21	29.36
r	RNZ83-05*	144.60	203.33	1.21	bdl	16.08	2.47	0.35	37.03	25.24
c	RNZ83-06*	60.00	131.54	1.39	0.04	10.12	0.92	0.15	21.14	24.11
r	RNZ83-09*	122.52	219.32	1.15	bdl	15.31	1.75	0.25	38.27	26.93

Table 3 continued

Domain	Sample	P	Y	*HfO*$_2$ (wt%)	La	Ce	Sm	Eu	Dy	Lu
Separation Point: Rocky Granodiorite										
c	RNZ87-06	115.69	144.18	1.04	0.06	10.80	1.33	0.27	25.85	19.19
c	RNZ87-07	171.25	305.47	0.95	bdl	11.40	5.08	0.92	62.33	29.39
c	RNZ87-09	948.84	244.01	0.92	14.66	31.22	6.08	0.99	49.81	24.81
c	RNZ87-12	122.07	273.69	0.96	0.06	12.47	4.42	0.82	55.26	27.80
r	RNZ87-01	100.45	127.88	1.15	bdl	13.02	1.02	0.19	22.49	17.34
r	RNZ87-04	100.94	105.31	1.14	0.03	11.48	0.80	0.19	17.79	15.42
r	RNZ87-05	113.28	158.69	1.04	bdl	10.84	1.41	0.29	28.67	20.37
r	RNZ87-08	95.20	110.53	1.16	bdl	12.69	0.86	0.18	18.92	15.69
r	RNZ87-10	115.18	115.01	1.00	bdl	9.66	1.01	0.22	20.26	14.34
r	RNZ87-11	1611.34	187.78	1.10	13.96	41.98	4.22	0.58	34.01	24.29
c	RNZ87-03*	279.61	325.43	1.29	0.03	24.07	1.28	0.18	48.88	43.45
Titiroa Granite										
c	TT6-01	161.52	572.91	1.17	0.10	21.29	2.90	0.85	48.74	36.61
c	TT6-03	223.96	1598.33	1.06	0.08	15.97	4.92	2.50	130.37	99.94
c	TT6-09	90.87	546.09	1.26	0.06	18.03	2.27	0.73	45.48	36.27
c	TT6-11	283.74	1472.34	1.14	bdl	23.11	5.24	2.65	123.00	70.62
c	TT6-12	187.84	1058.20	1.43	0.13	23.09	2.76	0.89	81.23	65.95
c	TT6-14	306.05	1999.86	0.97	0.03	19.83	5.97	3.53	160.16	116.17
c	TT6-16	78.36	453.68	1.13	0.03	20.99	1.53	0.47	37.54	27.78
c	TT6-19	74.11	546.11	1.14	0.08	26.07	1.93	0.57	43.26	31.44
c	TT6-20	126.15	811.73	1.13	0.43	33.44	3.94	1.03	67.74	43.88
r	TT6-06	219.38	1025.32	1.40	2.30	25.66	8.55	4.78	86.63	71.06
r	TT6-13	785.89	3939.45	1.53	0.16	59.92	9.67	2.39	324.12	162.57
r	TT6-15	353.89	1557.08	1.22	0.04	32.89	5.84	1.68	136.88	82.10
r	TT6-17	249.89	1722.07	1.05	0.05	31.95	4.18	1.81	135.36	87.10
r	TT6-18	721.64	331.78	1.25	4.98	28.63	2.74	0.74	29.60	23.33
r	TT6-02*	91.88	311.23	1.43	1.30	16.18	5.15	1.90	29.56	21.48
r	TT6-04*	620.11	3530.68	1.26	0.03	39.03	10.11	3.97	312.97	163.38
c	TT6-05*	239.40	1119.73	1.20	0.05	16.35	3.74	0.80	89.45	71.57
c	TT6-07*	177.68	588.00	1.19	bdl	8.44	1.66	0.42	46.64	38.99
r	TT6-08*	445.78	3056.63	1.21	2.00	69.09	20.18	6.89	311.39	109.51
r	TT6-10*	222.78	1498.03	1.98	5.28	52.32	21.18	8.45	138.75	73.36
r	TT6-21*	797.34	2107.03	2.00	0.02	9.24	2.19	0.52	156.22	118.79
North Fiord Granite										
c	NF3-04	91.54	732.35	1.21	bdl	31.96	2.50	0.85	63.97	46.80
c	NF3-05	148.20	554.77	1.21	bdl	14.23	1.73	0.62	47.92	36.36
c	NF3-07	219.01	1722.57	1.24	bdl	60.89	6.08	2.15	156.51	83.77
c	NF3-09	122.55	999.13	1.19	bdl	32.76	3.14	1.11	90.95	52.02
c	NF3-14	43.21	177.53	1.19	0.06	6.93	0.58	0.20	14.06	14.44
c	NF3-16	115.43	867.38	1.04	0.03	31.34	3.51	1.32	78.30	47.05
c	NF3-18	106.96	810.87	1.16	0.03	21.57	2.46	0.90	68.74	49.02
c	NF3-20	254.50	2174.66	1.06	0.67	119.96	30.23	9.82	238.25	81.73
c	NF3-22	127.10	456.96	1.17	0.07	13.35	1.59	0.61	39.17	31.76
r	NF3-02	73.28	503.59	1.18	bdl	23.55	2.24	0.84	45.27	31.62
r	NF3-06	195.96	1394.06	1.40	bdl	41.11	3.42	1.07	117.80	76.83
r	NF3-08	327.32	2456.60	1.46	bdl	82.56	5.90	1.33	213.73	120.57
r	NF3-11	183.55	1093.33	1.41	bdl	51.98	4.37	1.27	100.95	51.45

Table 3 continued

Domain	Sample	P	Y	HfO_2 (wt%)	La	Ce	Sm	Eu	Dy	Lu
r	NF3-13	111.54	1202.25	1.23	0.03	34.33	2.97	1.09	101.44	64.68
r	NF3-15	165.29	1170.35	1.40	0.03	29.76	2.74	0.89	96.82	67.63
r	NF3-21	142.69	1206.78	1.38	0.05	38.96	2.73	0.99	92.91	77.30
r	NF3-10*	640.39	3559.31	1.83	0.05	67.89	6.94	1.38	299.78	178.65
c	NF3-12*	390.54	1400.31	1.08	0.05	20.25	6.20	0.76	123.02	78.87
r	NF3-17*	207.12	1601.72	1.10	0.12	93.82	11.39	3.48	166.73	59.01
r	NF3-19*	183.43	1127.16	1.28	0.06	56.15	4.88	1.42	104.91	53.23
r	NF3-23*	206.28	1580.48	1.34	bdl	64.08	5.90	1.76	143.45	74.96
Takahe Granodiorite										
c	SF2a-03	1021.93	3193.21	1.20	0.03	30.99	11.88	3.76	348.64	126.51
c	SF2a-12	354.67	1131.90	1.06	0.13	18.51	3.14	0.40	93.72	71.33
c	SF2a-19	135.99	1095.88	1.14	bdl	26.50	3.11	1.18	98.24	48.86
r	SF2a-02	147.79	1242.75	1.21	bdl	27.45	3.09	0.84	106.51	61.90
r	SF2a-04	338.75	1738.66	2.01	0.09	24.29	3.80	0.62	141.63	96.16
r	SF2a-06	257.47	1291.12	1.18	bdl	51.62	4.69	1.03	122.39	57.78
r	SF2a-08	161.23	974.43	1.46	0.08	16.87	1.98	0.51	79.98	57.38
r	SF2a-10	177.08	1173.52	1.23	bdl	33.74	3.68	0.93	107.20	55.29
r	SF2a-13	975.17	1969.63	1.08	1.70	102.34	13.12	3.69	208.83	69.20
r	SF2a-14	157.58	1009.48	1.27	bdl	17.89	2.06	0.52	80.67	59.63
r	SF2a-15	501.69	2628.27	1.18	0.20	102.25	14.84	3.95	269.96	87.08
r	SF2a-16	566.77	2863.71	2.55	9.13	161.27	117.46	22.00	289.90	143.17
r	SF2a-17	109.42	559.28	1.22	bdl	9.66	1.10	0.36	48.98	31.06
r	SF2a-18	87.63	1028.38	1.09	bdl	26.63	3.03	1.27	88.02	48.90
r	SF2a-20	491.21	1634.77	1.26	0.15	22.40	3.96	0.81	139.59	71.59
c	SF2a-01*	236.02	899.68	0.86	0.04	5.25	2.87	0.56	80.71	60.24
c	SF2a-05*	104.99	275.24	1.08	0.03	3.64	0.75	0.15	22.65	19.91
c	SF2a-07*	125.86	385.73	1.11	bdl	5.87	0.68	0.13	29.96	32.79
c	SF2a-09*	261.87	968.94	1.04	0.09	12.73	3.08	0.42	79.53	65.58
r	SF2a-11*	4582.71	633.42	1.06	53.93	116.01	9.16	1.49	58.08	36.17
Western Fiordland Orthogneiss										
c	WF-01	145.85	817.58	0.94	0.09	12.44	8.88	1.38	84.16	37.49
c	WF-03	142.78	472.25	1.00	0.22	11.15	4.99	0.78	48.96	23.60
c	WF-05	184.00	1180.73	0.91	0.10	13.21	9.45	1.67	119.33	52.61
c	WF-08	159.83	642.24	0.92	0.06	10.91	6.60	1.08	67.08	30.24
c	WF-09	176.19	1195.86	0.91	0.12	13.33	9.22	1.55	114.77	52.15
c	WF-11	85.25	221.96	1.13	bdl	7.58	1.15	0.20	20.38	13.78
c	WF-14	163.67	431.46	0.92	0.04	9.27	3.98	0.66	44.35	21.42
c	WF-15	122.34	242.44	1.09	bdl	7.97	1.33	0.25	22.53	14.81
c	WF-18	127.98	631.64	0.97	0.06	12.21	7.89	1.21	69.17	28.15
c	WF-21	134.33	558.65	1.03	bdl	11.51	6.08	0.98	59.02	26.98
r	WF-02	136.29	656.35	0.95	0.05	10.99	6.98	1.11	70.03	30.88
r	WF-04	133.90	596.39	1.01	0.04	12.57	7.25	1.18	65.47	27.97
r	WF-06	175.91	1095.92	0.91	0.11	12.90	9.47	1.66	111.11	49.16
r	WF-07	165.82	355.83	0.95	bdl	9.22	2.83	0.52	36.87	18.36
r	WF-10	129.95	659.65	0.99	0.12	13.07	8.20	1.34	72.21	30.21
r	WF-12	127.45	678.56	1.10	bdl	12.86	3.86	0.67	64.19	36.75
r	WF-13	120.05	373.37	1.11	0.10	12.48	2.05	0.39	31.31	24.91
r	WF-16	121.87	345.29	1.07	bdl	10.65	1.40	0.30	29.48	21.57

Table 3 continued

Domain	Sample	P	Y	*HfO*$_2$ (wt%)	La	Ce	Sm	Eu	Dy	Lu
r	WF-17	125.90	659.28	1.07	0.04	13.06	6.54	0.97	66.81	32.71
r	WF-19	132.37	632.36	0.96	0.05	11.80	6.95	1.17	68.04	27.86
r	WF-22	103.87	251.43	1.06	0.03	8.18	1.84	0.30	24.58	14.33
r	WF-20*	132.12	293.90	1.00	0.08	10.84	2.20	0.49	28.58	15.96

* zircon spot analyses excluded from age calculations; *bdl* below detection limit

negative Eu anomalies, as Eu(III) is partitioned into the zircon lattice in strong preference to reduced Eu(II) (Fig. 10). Hence, increasing values of Ce(IV)/Ce(III) and $Eu_{N/}Eu_N$* (i.e. approaching the value of 1) in zircon denote higher magmatic oxidation states (e.g. Ballard et al. 2002; Hoskin and Schaltegger 2003). In the present study, increasing Ce(IV)/Ce(III) are accompanied by generally increasing $Eu_{N/}Eu_N$* in zircon in three of the studied granitoid samples (RNZ20, RNZ49 WFO1). Furthermore, highest values for both ratios are prevalent in the most evolved granitoids (RNZ20, RNZ49, NF3, TT6), suggesting that these granitoids reached highest levels of fO_2. Ballard et al. (2002) documented a systematic relationship between the age, degree of whole rock differentiation and the oxidation state of a suite of Cu-mineralised and unmineralised intrusive rocks from Chile. In analogy to their reasoning, it is suggested that in some of the most evolved SPS granitoids igneous differentiation was accompanied by an increase in the oxidation state.

In contrast to Ce(IV)/Ce(III), variability in $Eu_{N/}Eu_N$* is complicated by the effects of plagioclase crystallisation. Eu(II) is much more strongly partitioned into feldspar than Eu(III). At the same time, Eu speciation is directly controlled by the oxidation state of the magmatic system; hence, under reducing conditions, more Eu (II) is available to be incorporated into crystallising feldspar, resulting in a depletion of Eu in the melt. Conversely, if a granitic system undergoes progressive oxidation, lower quantities of Eu(II) are available to be scavenged by crystallising feldspar. This means that $Eu_{N/}Eu_N$* may not necessarily decrease in zircon in response to progressive oxidation and concomitant feldspar fractionation. In the present study, a significant role of feldspar fractionation is indicated by an increase in whole rock Rb/Sr ratios, as differentiation was driving the system(s) towards elevated SiO_2 and low Mg# (Fig. 11b, c). The effects of feldspar fractionation on zircon composition are resolvable in SPS samples RNZ20, TNZ83, SF2a and TT6, where progressive Eu depletion is accompanied by a decrease in *T* as a proxy of differentiation (Fig. 10). In addition, Eu and Ce systematics may be affected by open system processes, such as assimilation of feldspar-rich country rocks or replenishment by Eu-undepleted mafic melts. Assimilation may be detectable by a decrease in $Eu_{N/}Eu_N$* with increasing *T*, as feldspar-rich material is incorporated into the melt, although the effects on Ce(IV) and *T* co-variability remain difficult to assess. Crustal assimilation appears unlikely to have influenced Ce and Eu systematics in granitoid samples RNZ83, RNZ87 and WFO1 in view of their primitive whole rock compositions and the absence of inherited zircons. Recharge of the granitic reservoir by more mafic and hotter melts (Eu_N/Eu_N* $\sim$ 1) is plausibly indicated by a positive correlation between Eu systematics and *T* (Fig. 10), although this process would likewise be difficult to distinguish from feldspar fractionation.

In summarising the above discussion, zircons can evidently form under highly variable physico-chemical conditions during which the melt evolves via a series of igneous processes (Ballard et al. 2002; Coleman et al. 2004; Lowery-Claiborne et al. 2007), including fractional crystallisation, replenishment and wallrock assimilation, in addition to other complications arising from inheritence. Therefore, granitoid bulk rocks likely attain through crystallisation compositional, mineralogical and textural traits that may record late-stage processes and factors that operated just before solidification of a crystal mush. In consequence, zircon chemistry affords a more extended and detailed record of the petrogenetic history of plutonic systems.

Constraints on pluton assembly

As discussed previously., error-weighted mean ages for cores and rims for zircons from individual SPS granitoids

Fig. 10 Chondrite-normalised (Boynton 1984) REE diagrams for ▶ zircons from eight SPS/WFO granitods showing average compositions for cores and rims (*upper left diagrams*), individual analyses (*lower left diagrams*) and variability in Ce(III)/Ce(IV), $T_{(\text{Ti-in-zircon})}$ versus $Eu_{N/}Eu_N$* space. Ce(III)/Ce(IV) is the ratio of trivalent to tetravalent Ce in zircon calculated using a lattice strain model of mineral-melt partitioning (Ballard et al. 2002). $Eu_{N/}Eu_N$* was calculated through interpolation using neighbouring elements. All zircon spot analyses are shown for each plutonic sample, except data for inherited grains with ages » 130 Ma. Note that only five elements were measured, whereas the remaining elemental abundances were interpolated using the equations given in the "Analytical techniques"

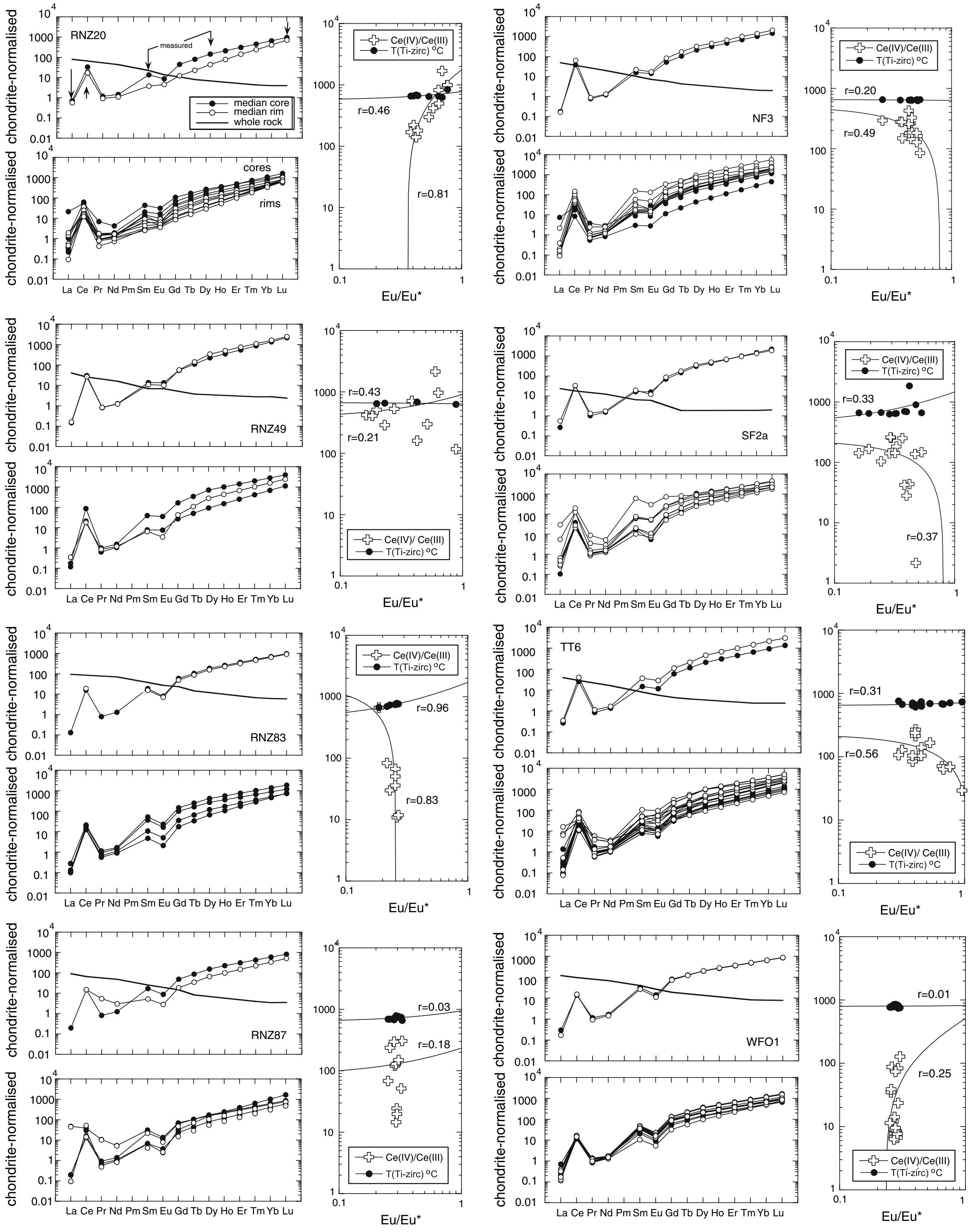

deviate by up to 5 myr., with the majority by ~2 myr. This is permissive of a scenario, whereby cores formed during earlier distinct stages in the magmatic evolution. On the basis of pooling age data alone, the core- and rim-forming events are statistically not resolvable, due to limitations arising from uncertainties in the LA-ICPMS data. This

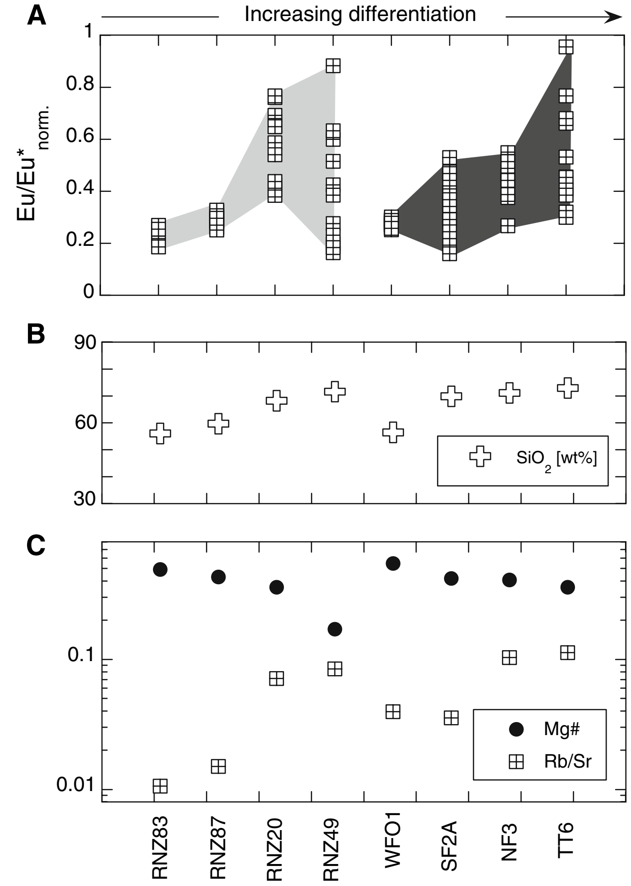

Fig. 11 **a** Variability in $\mathrm{Eu}_{\mathrm{N}}/\mathrm{Eu}_{\mathrm{N}}^*$ among zircons from SPS granitoids. Note that $\mathrm{Eu}_{\mathrm{N}}/\mathrm{Eu}_{\mathrm{N}}^*$ display a limited range at low values (<0.6) for the most primitive studies samples (RNZ83, 87, WFO1), while $\mathrm{Eu}_{\mathrm{N}}/\mathrm{Eu}_{\mathrm{N}}^*$ are highly variable in the more evolved granitoids. Low and high $\mathrm{Eu}_{\mathrm{N}}/\mathrm{Eu}_{\mathrm{N}}^*$ may indicate continuing feldspar fractionation and mixing of evolved crystal mush with mafic melt injections. **b**, **c** Whole rock data (from Muir et al. 1995, 1998) revealing differentiation trends in SPS granitoids: increasing SiO_2, Rb/Sr and decreasing Mg# (molar Fe_2O_3/(molar Fe_2O_3 + MgO) translate into increasing degrees of igneous differentiation

prompted a more detailed examination of the age distribution within individual zircons in an attempt to establish whether texturally distinct zircon growth domains yield resolvable age differences. Core–rim age data for individual grains are presented in Fig. 12. Expectedly, a large number of core–rim pairs plot in vicinity of an equiline (with a slope of unity) indicating that rims and cores crystallised more or less simultaneously within analytical error. Four of all core–rim data pairs plot below the equiline, translating into older ages for the rims relative to the respective cores. Apparent "age reversals" are difficult to explain and may be related to (diffusive?) transfer of radiogenic Pb from core to rim. In the present study, repeated dissolution and co-precipitation of zircon is consistent with resolvable temperature fluctuations. Importantly, Fig. 12 documents that 9 (Nelson) and 10 (Fiordland) core–rim pairs differ in calculated ages by significantly more (i.e. >2 myr.) than the estimated errors for individual spot analyses, which is typically in the order of 1 myr. This difference in crystallisation age is robust and significant in view of the estimated errors obtained on the pooled age of the 91500, which is <1%. With respect to individual spot analyses a 1% error on ca. 120 Ma ages translates into ca. 1 myr. Thus, the zircon record resolves distinct time periods during which cores and rims were formed, well beyond the analytical uncertainty.

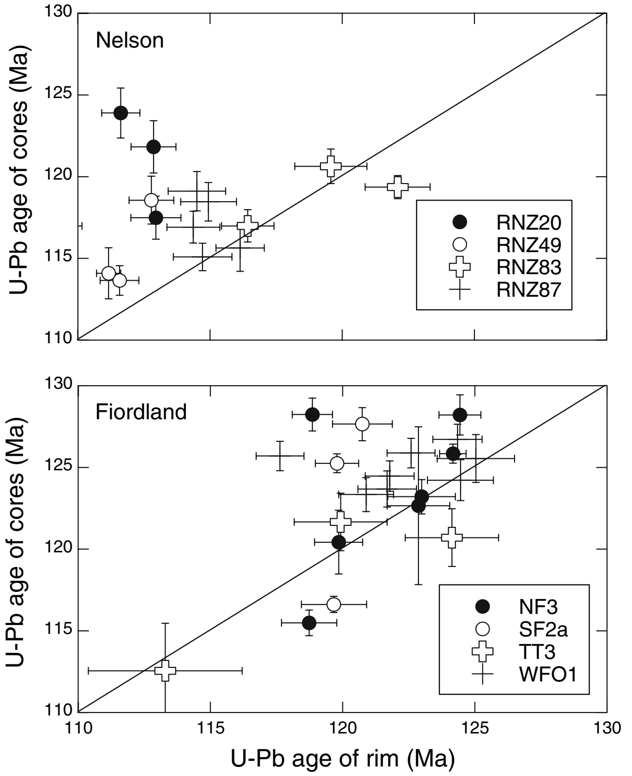

Fig. 12 Binary diagram showing U/Pb ICPMS ages for cores and rims obtained for individual zircons. Some core–rim ages plot below the equiline (slope of unity), implying that rims appear older than cores, contradicting textural observations that rims were accreted onto older cores. Importantly, a significant proportion of all analysed grains have rims that are significantly younger than cores, well beyond analytical uncertainty. Errors are shown as 1σ. Only magmatic zircons (i.e. excluding inheritence) with ages that appear unaffected by Pb loss are represented

The compilation of core–rim age relationships for individual zircons provides strong evidence that zircon crystallisation occurred over periods of time longer than the predicted thermal lifetimes of large magmatic bodies. Thermal models necessitate crustal magma bodies to cool below the solidus within only hundreds of thousands or even just several thousands of years. As an example, Glazner et al. (2004) estimated that a two-dimensional (5 × 20 km^2) hypothetical pluton would cool from 900°C below 750°C (taken as the point at which magma becomes immobile) within 500 ky. The present study supports a growing view that plutons are incrementally assembled over periods of several millions of years. For instance, Matzel et al. (2006) used high-precision single-grain TIMS U–Pb geochronology to document distinct age domains within plutons of the North Cascades, consistent with pluton construction over 5.5–2.6 myr. This finding, in combination with observed geochemical and textural variations, internal magmatic zoning and evidence for local magma mingling, was used by Matzel et al. (2006) to argue for pluton construction by amalgamation of multiple magma batches. Protracted emplacement of plutonic systems over periods of time of >10 myr. was also postulated by Coleman et al. (2004), who undertook detailed zircon geochronology on Late Cretaceous intrusive suites emplaced in the Sierra Nevada. In their study, zircon crystallisation ages were found to decrease systematically towards the centre of plutonic suites, which, along with field evidence for sheet-like emplacement along plutonic margins, negates the possibility that the pluton ever existed as a single magma chamber. In summarising the above information, we note that there is an increasing body of textural, thermal and geochronological evidence to suggest that plutonic systems may not intrude into the crust as a single batch of magma, but instead amalgamate from multiple, discrete intrusions.

In view of presented evidence it appears possible that age differences between cores and rims for SPS granitoids may also conform to models describing plutonic systems as multi-pulse, composite in structure. Incremental pluton assembly, punctuated by repeated remelting and resorption of zircons has been also reported for a 0.7–0.5 Ma rhyolite from the Coso Volcanic field (Miller and Wooden 2004). Therein, zircons extracted from a single rock showed pronounced age heterogeneity, interpreted by Miller and Wooden (2004) to represent multiple batches of rhyolite that were partially to completely solidified prior to remelting, possibly in response to thermal rejuvenation by emplacement of basaltic magma into the magmatic system. It was noted in that study that rhyolite eruption may have been triggered by fresh basaltic input. Similar mechanisms may apply to the magmatic evolution of SPS granitoids, as zircons show evidence for geochemical disequilibrium and resorption, in addition to age diachronism observed for cores and rims. Zircon cores may represent crystallisation products during initial accumulation of the magma or crystal mush. Subsequent reactivation during recharge by mafic input may have caused partial dissolution of existing zircon, followed by precipitation of new zircon in the form of rims.

Evidence for a multi-stage evolution of SPS/WFO plutons also comes from Zr/Hf–Th/U–T relationships. Whereas the more mafic plutons (RNZ83, RNZ87, WFO1) have relatively simple zircon crystallisation histories, consistent with these granitoids representing undisturbed (=higher melting point) cumulates, the lower *T*, more felsic (evolved) plutons have complex zircon histories, characterised by inheritence and a lack of simple Zr/Hf–Th/U–T relationships. These evolved granitoids must have experienced multiple cycles of rejuvenation and replenishment by new batches of hotter, more mafic magma.

Conclusions

Detailed CL imaging of zircons, coupled with LA-ICPMS U–Pb dating, trace element analysis and Ti-in-zircon thermometry, was employed to investigate the timing and crystallisation history of plutonism that gave rise to the Separation Point Suite in Nelson and Fiordland. More specifically, the results from the present study allow the following conclusions to be drawn:

- Weighted mean ages range from 112 ± 2 to 124 ± 1 Ma, in good agreement with previously published SHRIMP zircon ages obtained for the same granitoid rocks.
- Age inheritance spectra reveal subtle peaks at 500–600 and 1,050 Ma, and a dominant peak at 130–150 Ma. The youngest inherited component is most prevalent in the samples from eastern Fiordland and was probably derived from interaction with 170–130 Ma Darran Suite granitoids during emplacement of SPS magmas at mid-crustal levels. Older age components are restricted to the granitoids from Nelson and are likely to be inherited from Paleozoic metasedimentary rocks. The variability in zircon inheritance age spectra between both provinces strongly argues for emplacement-level contamination.
- Normalised REE patterns of zircon from individual plutons prove to be invariant towards compositional changes of the crystallising melt. This contrasts somewhat with clear trends of Zr/Hf and Th/U in zircon as a function of cooling. Relative abundances of the redox-sensitive rare earth elements Eu and Ce, on the other hand, provide evidence for progressively higher magmatic oxidation states as the silicic magmas evolve. Ubiquitous negative, but variable Eu anomalies in zircon require a combination of feldspar fractionation and magma oxidation, consistent with the co-variability of Eu_N/Eu_N^* and whole rock differentiation trends.
- Decreasing zircon Th/U and Zr/Hf ratios are highly correlated with temperature, consistent with progressive fractionation by accessory minerals that incorporate these incompatible elements. However, highly variable Th and U concentrations in zircon from more felsic samples, along with textural evidence for

repeated dissolution and subsequent regrowth, suggests that zircon resided in both saturated and undersaturated environments. Core to rim variations in crystallisation temperature and temperature reversals from core to rim, in particular, as revealed by Ti-in-zircon thermometry, also point to a complex history during which fractional crystallisation was punctuated by episodes of increased heat flux, probably in response to recharge by hotter, more mafic magmas.

- A significant number of zircons from SPS plutons contain cores that formed ca. >2 myr. earlier than the respective rims, which is outside uncertainty for individual spot analyses. Extended periods of zircon crystallisation violate thermal models, which predict medium-sized plutonic systems to cool below solidus within several 100 ky, assuming closed-system behaviour. On this basis, it is proposed that the SPS plutons were not emplaced into the crust as single magma chambers. Instead, early zircon now present as cores were formed during initial accumulation of magma or crystal mush. Subsequently, these zircons were partially dissolved due to thermal rejuvenation and replenishment by hotter, more mafic magma, followed by precipitation of new zircon to form the rims once thermal and chemical conditions allowed zircon saturation to re-establish.

Acknowledgments This research was funded through a Marsden grant to JWC and SDW and a University of Otago Research Grant to JMP. RB acknowledges a postdoctoral fellowship from the University of Canterbury. Charlotte Allen and Mike Shelley (Australian National University) and Michelle Herd, Rob Spiers, Jennifer Jackson, Kerry Swanson and Sacha Baldwin-Cunningham (University of Canterbury) are thanked for assistance with ICPMS analysis and mineral separation. Constructive and detailed criticism by two anonymous reviewers as well as editorial input from Bill Collins helped to improve the clarity of this paper. Anekant Wandres provided an electronic copy of the geological map and helpful advice.

References

Ballard JR, Palin JM, Williams IR, Campbell IH (2001) Two ages of porphyry intrusion resolved for the super-giant Chuquicamata copper deposit in northern Chile by ELA-ICPMS. Geology 29:383–386

Ballard JR, Palin JM, Campbell IH (2002) Relative oxidation states of magmas inferred from Ce(IV)/Ce(III) in zircon: application to porphyry copper deposits of northern Chile. Contrib Mineral Petrol 144:347–364

Bateman R (1995) The interplay between crystallisation, replenishment, and hybridization in large felsic magma chambers. Earth Sci Rev 39:91–106

Black LP, Kamo SL, Allen CM, Aleinikoff JN, Davis DW, Korsch RJ, Foudoulis C (2003) TEMORA 1: a new zircon standard for Phanerozoic U–Pb geochronology. Chem Geol 200:155–170

Blundy J, Wood B (1994) Prediction of crystal-melt partition coefficients from elastic moduli. Nature 372:452–454

Bolhar R, Whitehouse MJ, Weaver SD, Cole JW (2006) Geochemical variability of zircons from the Cretaceous Separation Point Batholith (New Zealand)—clues to sources and igneous processes. Geochim Cosmochim Acta 70(18):A57–A57

Bolhar R, Weaver SD, Whitehouse MJ, Palin JM, Woodhead JD, Cole JW (2008) Sources and evolution of arc magmas inferred from coupled O- and Hf-isotope systematics of plutonic zircons from the Cretaceous Separation Point Suite (New Zealand). Earth Planet Sci Lett (accepted)

Boynton WV (1984) Geochemistry of the rare earth elements: meteorite studies. In: Henderson P (ed) Rare earth element geochemistry. Elsevier, Amsterdam, pp 63–114

Bradshaw JD (1989) Cretaceous geotectonic pattern in the New Zealand region. Tectonics 8:803–820

Cavosie AJ, Valley JW, Wilde SA, EIMF (2006) Correlated microanalysis of zircon: Trace element, δ^{18} O, and U–Th–Pb isotopic constraints on the igneous origin of complex >3900 Ma detrital grains. Geochim Cosmochim Acta 70:5601–5616

Charlier BLA, Wilson CJN, Lowenstern JB, Blake S, Calsteren PWV, Davidson JP (2005) Magma generation at a large, hyperactive silicic volcano (Taupo, New Zealand) revealed by U–Th and U–Pb systematics in zircons. J Petrol 46:3–32

Coleman DS, Gray W, Glazner AF (2004) Rethinking the emplacement and evolution of zoned plutons: geochronologic evidence for incremental assembly of the Tuolumne Intrusive Suite, California. Geology 32:433–436

Compston W, Williams IS, Meyer C (1984) U–Pb geochronology of zircons from lunar breccia 73217 using a sensitive high mass-resolution ion microprobe. J Geophys Res 89(suppl):B525–B524

Davidson JP, Tepley III F, Knesel KM (1998) Crystal isotope stratigraphy: a method for constraining magma differentiation pathways. EOS 79:185, 189, 193

Davidson JP, Tepley III F, Palacz Z, Meffan-Main S (2001) Magma recharge, contamination and residence times revealed by in situ laser ablation analysis of feldspar in volcanic rocks. Earth Planet Sci Lett 184:427–442

Duffield WA, Ruiz J (1992) Compositional gradients in large volume reservoirs of silicic magma as evidenced by ignimbrites versus Taylor Creek Rhyolite lava domes. Contrib Mineral Petrol 110:192–210

Elburg MA (1996) U–Pb ages and morphologies of zircon in microgranitoid enclaves and peraluminous host granite: evidence for magma mingling. Contrib Mineral Petrol 123:177–189

Evans OC, Hanson GN (1993) Accessory-mineral fractionation of rare-earth element (REE) abundances in granitoid rocks. Chem Geol 110:69–93

Ferry JM, Watson EB (2007) New thermodynamic models and revised calibrations for the Ti-in-zircon and Zr-in-rutile thermometers. Contrib Mineral Petrol 154(4):429–437

Francalanci L, Davies GR, Lustenhouwer W, Tommasini S, Mason PRD, Conticelli S (2005) Intra-grain Sr isotope evidence for crystal recycling and multiple magma reservoirs in the recent activity of stromboli volcano, southern Italy. J Petrol 46:1997–2021

Gagnevin D, Daly JS, Waight TE, Morgan D, Poli G (2005) Pb isotopic zoning of K-feldspar megacrysts determined by Laser Ablation Multi-Collector ICP-MS: insights into granite petrogenesis. Geochim Cosmochim Acta 69:1899–1915

Gibson GM, Ireland TR (1995) Granulite formation during continental extension in Fiordland, New Zealand. Nature 375:479–482

Gibson GM, McDougall I, Ireland T (1988) Age constraints on metamorphism and the development of a metamorphic core complex in Fiordland, southern New Zealand. Geology 16:405–408

Glazner AF, Bartley JM, Coleman DS, Gray W, Taylor RZ (2004) Are plutons assembled over millions of years by amalgamation from small magma chambers? GSA Today 14:4–11

Griffin WL, Wang X, Jackson SE, Pearson NJ, O'Reilly SY, Xu XS, Zhou XM (2002) Zircon chemistry and magma mixing, SE China: in-situ analysis of Hf isotopes, Tonglu and Pingtan igneous complexes. Lithos 61(3–4):237–269

Harrison TM, McDougall I (1980) Investigation of an intrusive contact, northwest Nelson, New Zealand—1. Thermal, chronological and isotopic constraints. Geochim Cosmochim Acta 44:1985–2003

Harrison TM, Watson EB (1983) Kinetics of zircon dissolution and zirconium diffusion in granitic melts of variable water content. Contrib Mineral Petrol 84:66–72

Hawkesworth CJ, Kemp AIS (2006) Using hafnium and oxygen isotopes in zircons to unravel the record of crustal evolution. Chem Geol 226(3–4):144–162

Hollis JA, Clarke GL, Klepeis KA, Daczko NR, Ireland TR (2004) The regional significance of Cretaceous magmatism and metamorphism in Fiordland, New Zealand, from U–Pb zircon geochronology. J Metamorph Geol 22:607–627

Hoskin PWO (2005) Trace-element composition of hydrothermal zircon and the alteration of Hadean zircon from the Jack Hills, Australia. Geochim Cosmochim Acta 69(3):637–648

Hoskin PWO, Black LP (2000) Metamorphic zircon formation by solid-state recrystallization of protolith igneous zircon. J Metamorph Geol 18(4):423–439

Hoskin PWO, Ireland TR (2000) Rare earth element chemistry of zircon and its use as a provenance indicator. Geology 28(7):627–630

Hoskin PWO, Schaltegger U (2003) The composition of zircon and igneous and metamorphic petrogenesis. In: Hanchar JM, Hoskin PWO (eds) Zircon Reviews in Mineralogy and Geochemistry, vol 53. Mineralogical Society of America, Washington, pp 27–62

Hoskin PWO, Kinny PD, Wyborn D, Chappell BW (2000) Identifying accessory mineral saturation during differentiation in granitoid magmas: an integrated approach. J Petrol 41(9):1365–1396

Ireland TR (1992) Crustal evolution of New Zealand: evidence from age distributions of detrital zircon in Western Province paragneisses and Torlesse Greywacke. Geochim Cosmochim Acta 56:911–920

Jongens R, Bradshaw JD, Fowler A (2003) The Ballon Melange, northwest Nelson: origin, structure, and emplacement. NZ J Geol Geophys 46:437–448

Keay S, Steele D, Compston W (1999) Identifying granite sources by SHRIMP U–Pb zircon geochronology: an application to the Lachlan foldbelt. Contrib Mineral Petrol 137(4):323–341

Kemp AIS, Whitehouse MJ, Hawkesworth CJ, Alarcon MK (2005a) A zircon U–Pb study of metaluminous (I-type) granites of the Lachlan Fold Belt, southeastern Australia: implications for the high/low temperature classification and magma differentiation processes. Contrib Mineral Petrol 150(2):230–249

Kemp AIS, Wormald RJ, Whitehouse MJ, Price RC (2005b) Hf isotopes in zircon reveal contrasting sources and crystallisation histories for alkaline to peralkaline granites of Temora, southeastern Australia. Geology 33:797–800

Kimbrough DL, Tulloch AJ, Geary E, Coombs DS, Landis CA (1993) Isotopic ages from the Nelson region of South Island, New Zealand; crustal structure and the definition of the Median Tectonic Zone. Tectonophysics 225:443–448

Kimbrough DL, Tulloch AJ, Coombs DS, Landis CA, Johnston MR, Mattinson JM (1994) Uranium-lead zircon ages from the Median Tectonic Zone, South Island, New Zealand. NZ J Geol Geophys 37:393–419

Knesel KM, Davidson JP, Duffield WA (1999) Evolution of silicic magma through assimilation ans subsequent recharge: evidence from Sr isotopes in sanidine phenocrysts, Taylor Creek Rhyolite, NM. J Petrol 40:773–786

Kosler J, Fonneland H, Sylvester P, Tubrett M, Pedersen RB (2002) U–Pb dating of detrital zircons for sediment provenance studies—a comparison of laser ablation ICPMS and SIMS techniques. Chem Geol 182(2–4):605–618

Lowery-Claiborne L, Miller CF, Walker N, Wooden JL, Mazdab FK, Bea F (2007) Tracking magmatic processes through Zr/Hf ratios in rocks and Hf and Ti zoning in zircons: an example from the Spirit Mountain Batholith, Nevada. Mineral Mag 70:517–543

Maas R, Kinny PD, Williams IR, Froude DO, Compston W (1992) The Earth's oldest known crust: a geochronological and geochemical study of 3900–4200 Ma old detrital zircons from Mount Narryer and Jack Hills, Western Australia. Geochim Cosmochim Acta 56:1281–1300

Maas R, Nicholls IA, Greig A, Nemchin A (2001) U–Pb zircon studies of mid-crustal metasedimentary enclaves from the S-type Deddick Granodiorite, Lachlan Fold Belt, SE Australia. J Petrol 42(8):1429–1448

Mahood G, Hildreth W (1983) Large partition coefficients for trace elements in high-silica rhyolites. Geochim Cosmochim Acta 47:11–30

Mattinson JL, Kimbrough DL, Bradshaw JY (1986) Western Fiordland orthogneiss: Early Cretaceous arc magmatism and granultie facies metamorphism, New Zealand. Contrib Mineral Petrol 92:383–392

Matzel JEP, Bowring SA, Miller RB (2006) Time scale of pluton construction at differing crustal levels: examples from the Mount Stuart and Tenpeak intrusions, North Cascades, Washington. Geol Soc Am Bull 118:1412–1430

Miller JS, Wooden JL (2004) Residence, resorption and recycling of zircons in Devils Kitchen Rhyolite, Coso Volcanic Field, California. J Petrol 45:2155–2170

Mortimer N, Gans P, Calvert A, Walker N (1999) Geology and thermochronometry of the east edge of the Median Batholith (Median Tectonic Zone): a new perspective on Permian to Cretaceous crustal growth of New Zealand. Isl Arc 8:404–425

Muir RJ, Ireland TR, Weaver SD, Bradshaw JD (1994) Ion microprobe U–Pb zircon geochronology of granitic magmatism in the Western Province of the South-Island, New-Zealand. Chem Geol 113(1–2):171–189

Muir RJ, Weaver SD, Bradshaw JD, Eby GN, Evans JA (1995) The Cretaceous Separation Point Batholith, New-Zealand—granitoid magmas formed by melting of mafic lithosphere. J Geol Soc 152:689–701

Muir RJ, IrelandTR, Weaver SD, Bradshaw JD (1996) Ion microprobe dating of Paleozoic granitoids: Devonian magmatism in New Zealand and correlations with Australia and Antarctica. Chem Geol 127:191–210

Muir RJ, Ireland TR, Weaver SD, Bradshaw JD, Evans JA, Eby GN, Shelley D (1998) Geochronology and geochemistry of a Mesozoic magmatic arc system, Fiordland, New Zealand. J Geol Soc 155:1037–1052

Pearce NJG, Perkins WT, Westgate JA, Gorton MP, Jackson SE, Neal CR, Chenery SP (1997) A compilation of new and published major and trace element data for NIST SRM 610 and NIST SRM 612 glass reference materials. Geostand Newsl 21:115–144

Ramos FC, Reid MR (2005) Distinguishing melting of heterogeneous mantle sources from crustal contamination: insights from Sr isotopes at the phenocryst scale, Pisgah Crater, California. J Petrol 46:999–1012

Robinson DM, Miller CF (1999) Record of magma chambe processes preserved in accessory mineral assemblages, Aztec Wash pluton, Nevada. Am Mineral 84:1346–1353

Rubatto D (2002) Zircon trace element geochemistry: partitioning with garnet and the link between U–Pb ages and metamorphism. Chem Geol 184(1–2):123–138

Sawka WN (1988) REE and trace element variations in accessory minerals and hornblende from the strongly zoned McMurry Meadows Pluton, California. Trans R Soc Edinb Earth Sci 79:157–168

Scott JM, Cooper AF (2006) Early Cretaceous extensional exhumation of the lower crust of a magmatic arc: evidence from the Mount Irene Shear Zone, Fiordland, New Zealand. Tectonics 25:TC3018. doi:10.1029/2005TC001890

Stern RA, Amelin Y (2003) Assessment of errors in SIMS zircon U–Pb geochronology using a natural zircon standard and NIST SRM 610 glass. Chem Geol 197:111–142

Tepley III F, Davidson JP, Clynne MA (1999) Magmatic interactions as recorded in plagioclase phenocrysts of Chaos Crags, Lassen Volcanic Center, California. J Petrol 40:787–806

Tulloch AJ, Challis GA (2000) Emplacement depths of Paleozoic–Mesozoic plutons from western New Zealand estimated by hornblende-Al geobarometry. NZ J Geol Geophys 43:555–567

Tulloch AJ, Kimbrough DL (2003) Paired plutonic belts in convergent margins and the development of high Sr/Y: Peninsular Ranges batholith of Baja-California and Median batholith of New Zealand. Geol Soc Am Bull Spec Pap 374:275–295

Waight TE, Weaver SD, Muir RJ (1998) Mid-Cretaceous granitic magmatism during the transition from subduction to extension in southern New Zealand: a chemical and tectonic synthesis. Lithos 45(1–4):469–482

Wandres AM, Bradshaw JD (2005) New Zealand tectonostratigraphy and implications from conglomeratic rocks for the configuration of the SW Pacific margin of Gondwana. In: Vaughan APM, Leat PT, Pankhurst RJ (eds) Terrance processes at the margins of Gondwana, vol 246. The Geological Society of London, Special Publication, pp 179–216

Wark DA, Miller CF (1993) Accessory mineral behaviour during differentiation of a granite suite: monazite, xenotime and zircon in the Sweetwater Wash pluton, southeastern California, USA. Chem Geol 110:49–67

Watson EB, Harrison TM (2005) Zircon thermometer reveals minimum melting conditions on earliest. Earth Sci 308:841–844

Watson EB, Wark DA, Thomas JB (2006) Crystallisation thermometers for zircon and rutile. Contrib Mineral Petrol 151:413–433

Whitehouse MJ, Kamber BS (2005) Assigning dates to thin gneissic veins in high-grade metamorphic terranes: a cautionary tale from Akilia, southwest Greenland. J Petrol 46(2):291–318

Whitehouse MJ, Platt JP (2003) Dating high-grade metamorphism—constraints from rare-earth elements in zircon and garnet. Contrib Mineral Petrol 145(1):61–74

Wiebe RA (1993) The Pleasant Bay layered gabbro-diorite, coastal Maine; ponding and crystallisation of basaltic injections into a silicic magma chamber. J Petrol 34:461–489

Wiebe RA, Collins WJ (1998) Depositional features and stratigraphic sections in granitic plutons; implications for the emplacement and crystallisation of granitic magma. J Struct Geol 20:1273–1289

Wiebe RA, Smith D, Sturm M, King EM, Seckler MS (1997) Enclaves in the Cadillac Mountain Granite (Coastal Maine): samples of hybrid magma from the base of the chamber. J Petrol 38:393–423

Wiedenbeck M, Alle P, Corfu F, Griffin WL, Meier M, Oberli F, Vonquadt A, Roddick JC, Speigel W (1995) 3 Natural zircon standards for U–Th–Pb, Lu–Hf, trace-element and REE analyses. Geostand Newsl 19(1):1–23

Wiedenbeck M, Hanchar JM, Peck WH, Sylvester P, Valley J, Whitehouse M, Kronz A, Morishita Y, Nasdala L et al (2004) Further characterisation of the 91500 zircon crystal. Geostandards Geoanalytical Res 28:9–39

Williams IS, Chappell BW, Chen YD, Crook KAW (1992) Inherited and detrital zircons—vital clues to the granite protoliths and early igneous history of southeast Australia. Trans R Soc Edinb Earth Sci 83:503

Wysoczanski RJ, Gibson GM, Ireland TR (1997) Detrital zircon age patterns and provenance in Late Paleozoic to Early Mesozoic New Zealand; terranes and development of the Paleo-Pacific Gondwana margin. Geology 25:939–942

Zartman RE, Richardson SH (2005) Evidence from kimberlitic zircon for a decreasing mantle Th/U since the Archean. Chem Geol 220(3–4):263–283